Universiteit Antwerpen

This item is the archived peer-reviewed author-version of:

Fe^{2+} deficiencies, FeO subdomains, and structural defects favor magnetic hyperthermia performance of iron oxide nanocubes into intracellular environment

Reference:

Lak Aidin, Cassani Marco, Mai Binh T., Winckelmans Naomi, Cabrera David, Sadrollahi Elaheh, Marras Sergio, Remmer Hilke, Fiorito Sergio, Cremades-Jimeno Lucia, ...-Fe^{2+} deficiencies, FeO subdomains, and structural defects favor magnetic hyperthermia performance of iron oxide nanocubes into intracellular environment

Nano letters / American Chemical Society - ISSN 1530-6984 - 18:11(2018), p. 6856-6866

Full text (Publisher's DOI): https://doi.org/10.1021/ACS.NANOLETT.8B02722

To cite this reference: https://hdl.handle.net/10067/1554390151162165141

uantwerpen.be

Institutional repository IRUA

Fe^{2+} Deficiencies, FeO Sub-Domains, and Structural Defects Favor Magnetic Hyperthermia Performance of Iron Oxide Nanocubes into Intracellular Environment

Aidin Lak,† Marco Cassani,† Binh T. Mai,† Naomi Winckelmans,‡ David Cabrera,§ Elaheh Sadrollahi,# Sergio Marras,† Hilke Remmer,‖ Sergio Fiorito,† Lucia Cremades-Jimeno,§ Fred Jochen Litterst,# Frank Ludwig,‖ Liberato Manna,† Francisco J. Teran,§,⁋ Sara Bals,‡ Teresa Pellegrino*†*

†Istituto Italiano di Tecnologia, via Morego 30, 16163 Genoa, Italy

‡EMAT, University of Antwerp, Groenenborgerlaan 171, B-2020 Antwerp, Belgium

§iMdea Nanociencia, Campus Universitario de Cantoblanco, 28049 Madrid, Spain

#Institute of Condensed Matter Physics, Technische Universität Braunschweig, Mendelssohn-Str. 3, 38106 Braunschweig, Germany

‖Institute for Electrical Measurement Science and Fundamental Electrical Engineering, Technische Universität Braunschweig, Hans-Sommer-Str. 66, 38106 Braunschweig, Germany

⁋Nanobiotecnología (iMdea Nanociencia), Unidad Asociada al Centro Nacional de Biotecnología (CSIC), 28049 Madrid, Spain

KEYWORDS: Iron oxide nanocubes, Phase transformation, Intracellular Magnetic hyperthermia, Viscosity, Fe^{2+} deficiencies, Scanning transmission electron microscopy

ABSTRACT

Herein, by studying a stepwise phase transformation of 23 nm FeO-Fe_3O_4 core-shell nanocubes into Fe_3O_4, we identify a composition at which the magnetic heating performance of the nanocubes is not affected by the medium viscosity and aggregation. Structural and magnetic characterizations reveal the transformation of the FeO-Fe_3O_4 nanocubes from having stoichiometric phase compositions into Fe^{2+} deficient Fe_3O_4 phases. The resultant nanocubes contain tiny compressed and randomly distributed FeO sub-domains as well as structural defects. This phase transformation causes a tenfold increase in the magnetic losses of the nanocubes, which remains exceptionally insensitive to the medium viscosity as well as aggregation unlike similarly sized single-phase magnetite nanocubes. We observe that the dominant relaxation mechanism switches from Néel in fresh core-shell nanocubes to Brownian in partially oxidized nanocubes and once again to Néel in completely treated nanocubes. The Fe^{2+} deficiencies and structural defects appear to reduce the magnetic energy barrier and anisotropy field, thereby driving the overall relaxation into Néel process. The magnetic losses of the particles remain unchanged through a progressive internalization/association to ovarian cancer cells. Moreover, the particles induce a significant cell death after being exposed to hyperthermia treatment. Here, we present the largest heating performance that has been reported to date for 23 nm iron oxide nanoparticles under cellular and intracellular conditions. Our findings clearly demonstrate the positive impacts of the Fe^{2+} deficiencies and structural defects in the Fe_3O_4 structure on the heating performance under cellular and intracellular conditions.

Anisotropically shaped magnetic nanoparticles have attracted great attention in the last few years especially with regard to magnetic hyperthermia (MH) and magnetic particle imaging (MPI) applications.[1–4] Magnetic nanoparticle mediated MH is an emerging therapeutic approach which induces cancer cell death through heat damage, which has succeeded in retreating brain tumors in clinical trials.[5,6] Iron oxide based nanoparticles are an indispensable candidate for MH due to their biocompatibility (*i.e.* they are FDA approved) and biodegradability.[7] There has been significant progress in controlled syntheses of spherical, cubic, star-, and octapod-shaped iron oxide nanoparticles thanks to advancements in the thermal decomposition of organometallic precursors.[8–16] Over the last few years, a fairly good understanding of how the particle's morphological features depend on the synthesis conditions has been also acquired.

The thermal decomposition of iron-oleate, pioneered by Hyeon et al.,[8] is one of the most studied synthesis procedures due to its versatility and scalability. The biggest drawback of this synthesis is the formation of antiferromagnetic (AFM) FeO-ferrimagnetic (FiM) Fe_3O_4 core-shell (CS) particles caused by the reductive chemistry of the decomposition reaction.[17–24] Such core-shell nanoparticles, synthesized using iron-oleate[25] or other iron precursors,[26] have been characterized by a variety of advanced methods. It is known that the FeO phase deteriorates the overall magnetization of the particles, thus jeopardizing their hyperthermia efficacy. There have been handful of studies on resolving the issue by attempting to directly fabricate single Fe_3O_4 phase particles.[27,28] Recently, Chen et al.[29] have modified the iron-oleate decomposition pathway by adding aromatic ethers as co-solvents and synthesized single phase ferrimagnetic spherical nanoparticles. Unni et al.[30] have shown that, by adding molecular oxygen to the reaction's protective gas during the decomposition reaction, semi-spherical single phase iron oxide nanoparticles can be formed. Alternatively, other studies have also shown post-synthesis

oxidations of the FeO-Fe_3O_4 CS particles,[11] mostly at elevated temperatures in organic media.[31] It has been shown that structural defects like anti-phase boundaries in as-prepared and annealed particles form small domain-like regions, which account for the reduction in both the magnetic moment and the heating performances.[20,32]

An equally crucial feature of magnetic nanoparticles for use in intracellular hyperthermia is that they need to generate sufficient heat in the cellular space, regardless of whether they are immobile (intracellular viscosity η=50-140 mPa·s)[33] or clustered within endosomes. Recent studies have shown that the magnetic losses of particles strongly depend on their environment *e.g.* the immobilization and clustering and will be dramatically reduced (up to 90%) depending on the particle size, chemical composition, and aggregation inside the live cells.[34–38] Cabrera et al.[39] have exploited alternating-current (AC) hysteresis loop measurements to demonstrate that 24 nm magnetite nanocubes lose their high specific absorption rate (SAR) nearly entirely when dispersed in viscous media (~100 mPa·s). Theoretical studies have also described how the viscosity influences the magnetic heat dissipation of nanoparticles.[39–41] It would appear that magnetic nanoparticles with a perfect crystal structure and high magnetic anisotropy, thus relaxing via the Brownian mechanism, do not adequately fulfill intracellular hyperthermia requirements. In an attempt to overcome the intracellular magnetic losses and degradation, 15 nm aminosilane-coated iron oxide nanoparticles have been directly injected at the tumor site which aggregated and stayed in place for multiple treatments.[42] Although 15 nm nanoparticles are less dependent on the medium viscosity, they generate considerably less magnetic heat than bigger nanoparticles.[39,42,43] Thus far, despite being a highly relevant criterion, very few studies have been dedicated to engineering the magnetic relaxation mechanisms of iron oxide nanocubes in order to fabricate heat mediators, which generate large heat and concomitantly preserve it inside the cells. Moreover, the fact that

the magnetic nanoparticles that are utilized in intracellular MH and MPI experiments share the same nanomagnetism principles highlights the importance of designing novel magnetic nanoparticles as MPI/MH theranostic agents.[4,34,44] To this end, nanoparticles should be fabricated so that they can efficiently maintain the heating capacity in the intracellular environment. To date, there have not been any reports on such a particle system that can accomplish this. This poses an intriguing question: *could compositional deficiencies and structural defects in the particles favor their heating capacity into biological matrices?*

In this study, we tackle this specific question by performing a stepwise thermal treatment and phase transformation of 23 nm FeO-Fe_3O_4 CS nanocubes. The nanocubes transform from a CS structure to an Fe^{2+} deficient Fe_3O_4 phase, which have compressed FeO sub-domains and defects, through the thermal process. The SAR of the nanocubes increases significantly, yet it remains insensitive to the medium viscosity, clustering, and internalization to cells, unlike similarly sized iron oxide nanocubes that are produced *via* direct methods. Our findings demonstrate that the Fe^{2+} deficiencies and structural defects drive the overall relaxation to Néel rather than Brownian and hence favor the heating performance of the nanocubes in cellular or viscous environments.

Highly uniform FeO-Fe_3O_4 CS nanocubes with an edge length of 23 nm were synthesized by thermal decomposition of iron-oleate (Figure S1, refer to the electronic supporting information (ESI)).[8,18] The nanocubes were thermally treated at 80°C for set time intervals after being coated with polyethylene glycol (PEG) derivative polymers and being transferred into water (ESI, Scheme 1, and Table 1). Dynamic light scattering (DLS) measurements confirm that the particle's hydrodynamic size remains unchanged throughout the entire thermal treatment process in water (Figure S3, ESI). The magnetic heating performance of the particles, which was evaluated with the calorimetric measure of the SAR quantity, increases significantly as the particles are thermally

treated. The SAR, measured at 301 kHz and 24 kA/m, soars from 15 to 382 W/g_{Fe} upon 48 h of treatment (Figure 1a, a typical calorimetric SAR measurement is plotted in Figure S4). The SAR values obtained for aliquots taken at intermediate time intervals increase stepwise, suggesting a gradual shrinkage of the FeO and an enlargement of the Fe_3O_4 domains, respectively, as a result of a longer thermal treatment. The observed improvements are to be expected since the FeO phase is paramagnetic at room temperature and therefore it scarcely contributes to the magnetic losses (Scheme 1).

Scheme 1. Evolution of the structural, compositional, and magnetic configurations of the nanocubes through the thermal treatment process. The different spin colors indicate differently oriented domain-like regions.

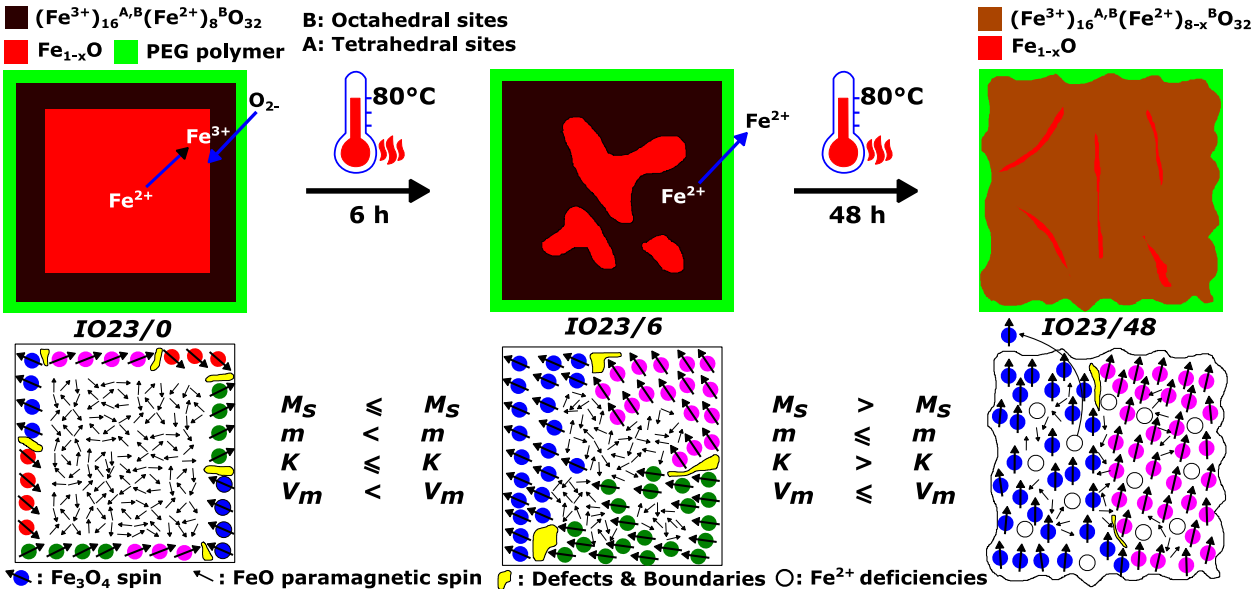

To elucidate the governing magnetic relaxation mechanism at each oxidation stage, we first performed SAR measurements at different medium viscosities (η) and matched these results with the results of the ac-susceptibility (ACS) measurements. These measurements enabled us to distinguish the Néel relaxation, which occurs when internal magnetic spins rotate from the Brownian relaxation which, in turn occurs through the rotation of the whole particle. The particles

were dispersed in 58.5:41.5 wt%, 27.2:72.8 wt%, and 15.7:84.3 wt% water-glycerol mixtures, corresponding to a mean η of 3.8, 23.0, 97.3 mPa·s.[39] Remarkably, the IO23/48 sample shows only a 15 to 18% drop in the SAR value at 301 and 100 kHz, respectively, when the viscosity increases by nearly two orders of magnitude, whereas the drop in the SAR value in the intermediate IO23/24 sample is significantly larger despite having a smaller magnetic volume V_m (Figure 1b). These results demonstrate that the IO23/48 nanocubes relax more dominantly *via* the Néel mechanism than the intermediately treated nanocubes. Note that the time constant τ_N depends exponentially on both the anisotropy constant K and the particle magnetic volume V_m (Eq. S10), and is independent of η. This seems counterintuitive to one's expectation, implying that particles with a larger V_m relax predominantly *via* the Brownian mechanism, in which the time constant τ_B depends linearly on both η and the particle hydrodynamic volume V_h (Eq. S9), therefore responding more drastically to η. The promising viscosity-independent magnetic heating performance of the IO23/48 sample is remarkable considering there is nearly a 100% SAR drop over a similar viscosity range for 24 nm magnetite nanocubes that are synthesized *via* a different heat-up protocol.[39] The findings suggest that the relaxation mechanism of the nanocubes is governed by other structural features, not just by the apparent physical sizes, which despite their subtlety are decisive.

To further verify the SAR results by applying magnetic measurements, AC hysteresis loops were recorded at 200 kHz for the IO23/48 nanocubes that were dispersed in similar water-glycerol mixtures. No significant changes in the hysteresis loop area (A) were observed when η was increased by two orders of magnitude, confirming that the SAR (*i.e.* proportional to $A \times f$)[45] is marginally dependent on the particle immobilization (Figures 1c and S5). The viscosity effect,

however, became more significant when lower field intensities were applied (Figure S6), which is in agreement with recent findings.[39]

The effect of particle clustering on the heating efficiency was further probed by increasing the particle's hydrodynamic size by adding BSA protein to the dispersion and recording the AC loops at 100 kHz (Figure 1d, Table S1). The hysteresis loop area A of the IO23/48 nanocubes drops merely by 34% when d_h increases from 74 to 114 nm, but it remains virtually constant for 810 nm clusters (Figure S5). Although the IO23/48 nanocubes reveal slightly higher aggregation effects on the SAR than the 20 nm maghemite nanoparticles reported by Ovejero et al.,[46] it is significant to highlight that the SAR of the IO23/48 in the aggregated state is two times higher than that of maghemite nanoparticles. The stronger aggregation effect is likely attributed to the larger core size of the IO23/48 nanocubes, which results into stronger intra-aggregate magnetic dipolar interactions. The maximum magnetization (M_{max}) and remanence magnetization (M_r) reduce by 20% as bigger clusters are formed. This indicates that the intra-aggregate dipole-dipole interactions lead to demagnetizing configurations in the clusters.

Table 1. Sample names, treatment conditions, edge length (L_c), number-weighted hydrodynamic diameter (d_h), polydispersity index (PDI), lattice constants (a_{RS} and a_S), and weight fraction of FeO and Fe_3O_4 phases extracted from TEM, DLS, and Rietveld analyses, respectively.

name	L_c (nm)	time(h)/temp.(°C)	d_h(nm)/PDI	a_{RS}/a_S(Å)	FeO/Fe_3O_4 (wt%)
IO23/0	23	0/---	43(3)/0.17	4.270(5)/8.432(5)	53(3)/47(3)
IO23/3	23	3/80	40(1) /0.14	4.259(5)/8.420(5)	36(3)/64(3)
IO23/6	23	6/80	40(2) /0.15	4.259(5)/8.410(5)	29(3)/71(3)
IO23/24	23	24/80	41(3) /0.14	---/8.390(3)	0/100
IO23/48	23	48/80	45(3) /0.19	---/8.385(3)	0/100

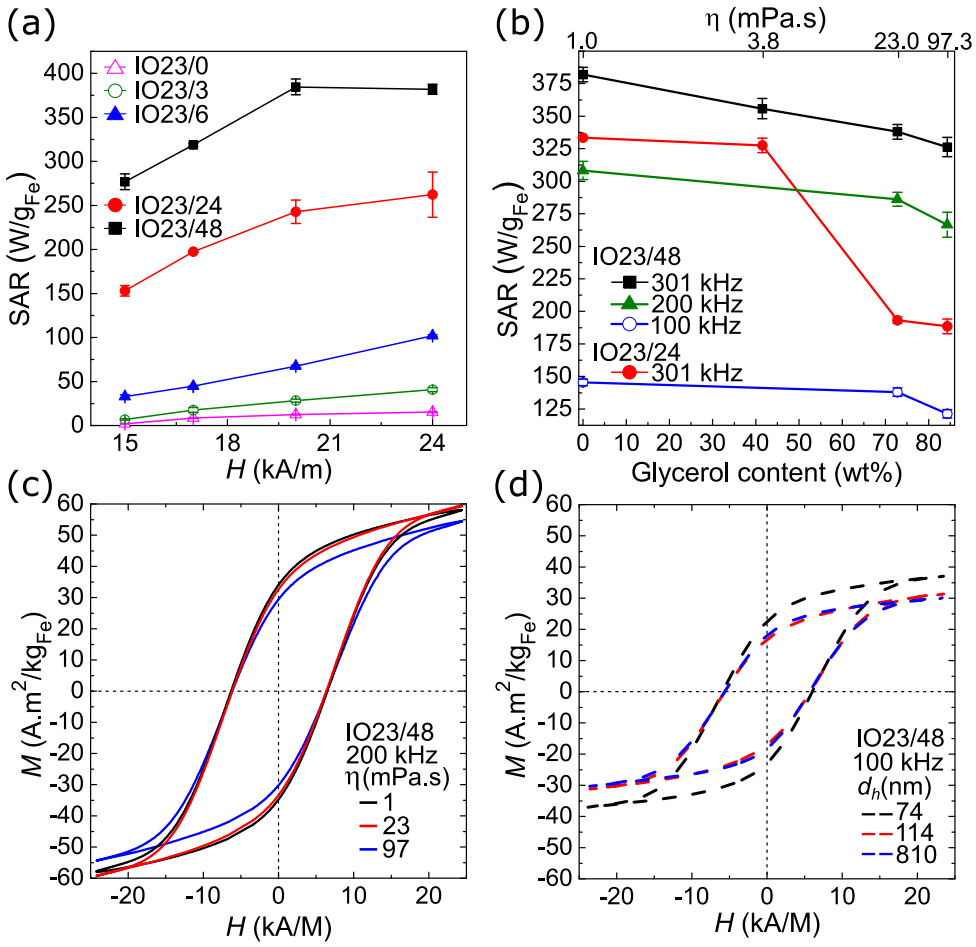

Figure 1. (a) Field dependence of the specific absorption rate (SAR) of 23 nm nanocubes that underwent the thermal treatment for different time intervals, measured at 301 kHz. (b) SAR evolution *vs.* glycerol content (wt%) and η, measured at 24 kA/m and 301, 200, and 100 kHz for IO23/48 and 301 kHz for IO23/24 nanocubes. (c) Effect of the medium viscosity η and (d) the particle cluster hydrodynamic size d_h on AC hysteresis loops of IO23/48 nanocubes, recorded at 200 and 100 kHz, respectively. The samples' characteristics are summarized in Table 1.

Complex ACS measurements were then carried out on all the samples in water and in water-glycerol mixtures in order to probe their magnetic relaxation mechanisms as well as their dependence on η. The imaginary part χ'' of the as-prepared CS nanocubes IO23/0 shows an appreciable double peak spectrum (marked with arrows in Figure 2a). The peak positioned at *ca.*

3 kHz can be unambiguously attributed to the Brownian relaxation, whereas the broad hump at *ca.*150 kHz is assigned to the Néel relaxation (Figure 2a). This means that in the IO23/0 sample $\tau_N < \tau_B$, and thus the Néel relaxation dominates. After 3 and 6 h of thermal treatment, the χ'' peak becomes symmetric and has no high frequency shoulder, indicating the domination of the Brownian process (*i.e.* $\tau_N > \tau_B$) in the IO23/3 and IO23/6 samples (Figure 2a). Remarkably, the χ'' peak becomes asymmetric towards high frequency regimes in the IO23/48 sample, indicating that $\tau_N < \tau_B$ and hence the Néel process contributes more significantly to the effective relaxation. The Néel shoulder can be easily appreciated by observing a pronounced double peak spectrum when the particles are dispersed in η=97 mPa·s (Figure 2b, green markers) wherein the Brownian and Néel relaxation frequencies are well separated. The peak assignment can be further confirmed by looking at the ACS spectra that were recorded at different viscosities (Figure 2b). The peak at 3 kHz moves gradually towards lower frequencies as η increases, as is to be expected for the Brownian relaxation. The hump at 150 kHz preserves its position, which is an intrinsic nature of the Néel relaxation.

These results suggest that there are intermediate structures (*i.e.* IO23/6) which behave in a more magnetically blocked manner than the IO23/48 nanocubes. This is an intriguing phenomenon which has not yet been reported. These findings fully support the viscosity dependent SAR behavior wherein a higher SAR drop was detected for the IO23/24. Remarkably, the viscosities estimated from the fits to the χ'' spectra (see Eq. S8, Figure 2b) match well with the values measured using a rheometer (Figure S7, ESI). This confirms the credibility of the applied model. These phenomena are quantitatively reflected in the magnetic energy barrier quantity KV_m which is derived from modelling the ACS spectra using the modified Debye model (Eq. S5, Figure S8, ESI). Interestingly, KV_m rises from the IO23/0 sample to the IO23/3 and IO23/6 samples,

indicating a switch in the dominant relaxation mechanism from the Néel to the Brownian mechanism during the initial oxidation stages (Figure S8). We hypothesize that the Fe_3O_4 domains grow towards the core more easily along disordered boundaries and defects, as they offer a higher ion diffusion rate. This could plausibly lead to the formation of a mosaic crystal structure with small FeO grains (Scheme 1) rather than a perfect planar growth of the FeO-Fe_3O_4 interface towards the core. The Fe_3O_4 domains that formed during the initial stages appear to possess a short-range cation/magnetic ordering and K quantity, which is closer to the bulk magnetite *i.e.* 11-13 kJ/m^3.[31] This leads to the domination of the Brownian mechanism in the IO23/6 particles. The KV_m decreases as the oxidation proceeds further, which is a strong indication of a larger contribution of the Néel mechanism to the effective relaxation. These trends were also reflected in the SAR *vs.* H plots (Figure S9). Noticeably, the SAR already saturates at H=20 kA/m for the IO23/48 sample, whereas it keeps rising linearly for the IO23/6 sample. These results indicate that there is a lower anisotropy field (H_A, given by $H_A=2K/M_s$) and K for the IO23/48 sample than for the IO23/6 one.

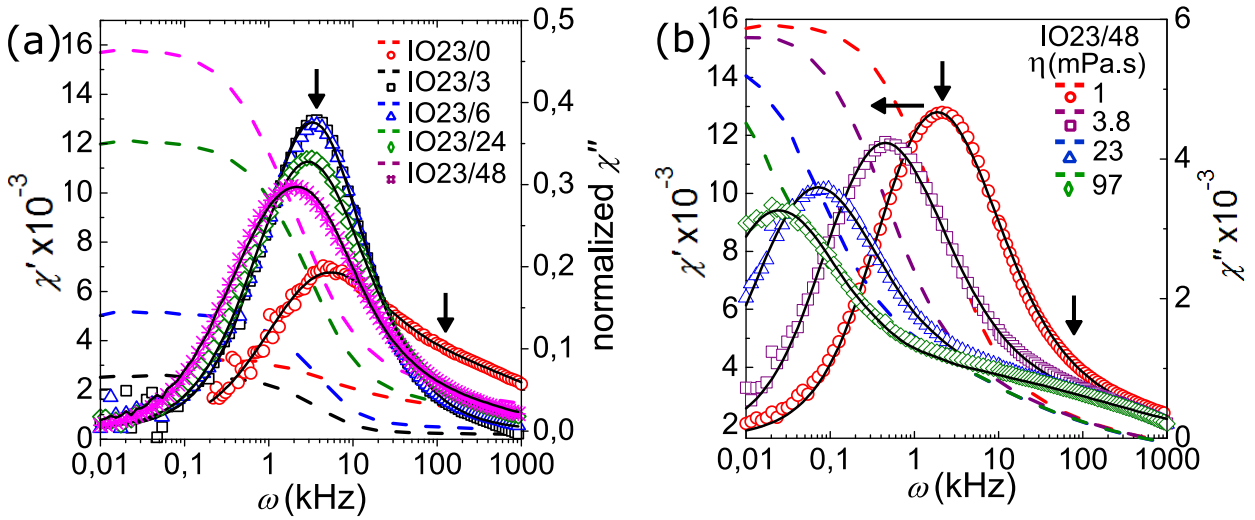

Figure 2. (a) Real (dashed lines) χ' and imaginary (markers) χ'' parts of complex ac-susceptibility spectra measured on IO23 sample series in water, and (b) on IO23/48 samples in different

viscosities (*i.e.* water-glycerol mixtures). The solid black lines are the best fits to χ'' using Eq. S5 and S8.

Additional insight was acquired by investigating the crystal structure of the particles using high angle annular dark field scanning transmission electron microscopy (HAADF-STEM). The intensity difference observed in the high resolution HAADF-STEM image (Figure 3a) suggests that the IO23/0 nanocubes have a CS structure. The Fast Fourier Transform (FFT) pattern acquired from the middle of the particle can be indexed to the [100] zone axis of FeO. Instead, the FFT pattern obtained near the edge can be indexed to the [100] zone of either magnetite (Fe_3O_4) or maghemite (γ-Fe_2O_3). The X-ray diffraction (XRD) pattern of the IO23/0 confirms the presence of both crystalline FeO and Fe_3O_4 phases (Figure 3b). The reflection positions coincide with $Fe_{0.942}O$ (ICSD: 98-002-4696, Rock-salt (RS)) and $Fe_{2.96}O_4$ (ICSD: 98-008-2443, Inverse spinel (S)), with a FeO:Fe_3O_4 phase ratio of 53:47 wt% based on the Rietveld analysis (Table 1, Table S3, and ESI).

The fine structure of monochromated electron energy loss spectroscopy (EELS) is used to differentiate between Fe^{2+} and Fe^{3+} valency, which enables us to distinguish between maghemite and magnetite. Based on the EELS maps, the core of the as prepared IO23/0 sample contains 88.9±6.2% Fe^{2+} (Figure S10, ESI). The small amount of Fe^{3+} detected at the core most likely originates from the shell on top and underneath. Near the edge of the nanoparticle, the shell contains twice as much Fe^{3+} (62.1±6.4%) as Fe^{2+}, which is characteristic of the Fe_3O_4 phase. These findings indicate that the IO23/0 nanocubes have a CS structure with sharp AFM-FiM interfaces.

A gradual evolution of the nanocubes from a biphasic system to a nearly single spinel phase after 48 h of thermal treatment can be seen by comparing the XRD patterns (Figure 3b), which were recorded at different time intervals (see Table 1 for a quantitative phase analysis). The FFT analysis

of the high resolution HAADF-STEM image of the IO23/48 sample (Figure 3c) reveals the disappearance of the CS structure. Nevertheless, it was possible to detect relatively small FeO sub-domains which had not been observed in the XRD pattern. These domains are randomly distributed throughout the entire particle, even on the shell (green rectangular in Figure 3c). Anti-phase boundary defects are also expected in these particles as they survive even higher annealing temperatures.[20,47]

From the Rietveld analyses of the XRD patterns, we have discerned that the lattice constants of FeO (a_{RS}, 4.270 Å) and Fe_3O_4 (a_S, 8.432 Å) in the IO23/0 sample decrease when the treatment time is prolonged, which is visually apparent through a shift in the reflection positions towards higher angles (*e.g.* $(311)_S$, $(400)_S$, and $(200)_{RS}$ reflections). A similar trend has been reported for a comparable system[20] and $Co_xFe_{1-x}O/Co_xFe_{3-x}O_4$ nanoparticles.[48] A decrease in a_S with respect to the nominal bulk value of magnetite is expected for Fe_3O_4, which indicates the release of the lattice expansion. The drop in the FeO lattice constant is, however, unexpected and suggests an accumulation of pressure on the FeO sub-domains as the oxidation progresses. This is presumably caused by the Fe_3O_4 domains which grow throughout the particles.[47] The GPa pressure range on the FeO domains substantially hampers the diffusion of Fe^{2+} towards outer layers, leading to the survival and migration of the FeO domains through the particles (Scheme 1).[20] According to the EELS valency maps (Figures 3d and 3e), the IO23/48 particles consist mainly of Fe^{3+} (84.4±7.1%), with some leftover Fe^{2+} (*ca.*16%). Compared with the nominal Fe^{3+}/Fe^{2+} ratio in magnetite (*i.e.* 66% versus 34%), this result suggests *ca.* 18% Fe^{2+} deficiencies.

Tilt series of HAADF-STEM images of the nanocubes were used as an input for a 3D reconstruction. It then became clear that the IO23/0 particles have a cubic shape with a smooth surface (Figure 3f). After the full thermal treatment, the morphology of the particle surface is more

rough (Figure 3g). It is known that nanoparticles that have a reduced valency, *e.g.* FeO and $Co_xFe_{1-x}O$, become bigger when they are oxidized due to the adsorption of a considerable amount of oxygen.[48] The formation of small hills and valleys on the particle surface may be an indication of particle growth. The shape of the IO23/48 nanocubes falls between a perfect cube and a sphere as a result of the surface roughness and rounded edges. This leads to the reduction of shape anisotropy and eventually the effective K and H_A quantities, driving the dominating spin relaxation to the Néel process and favoring the heating in viscous environments.

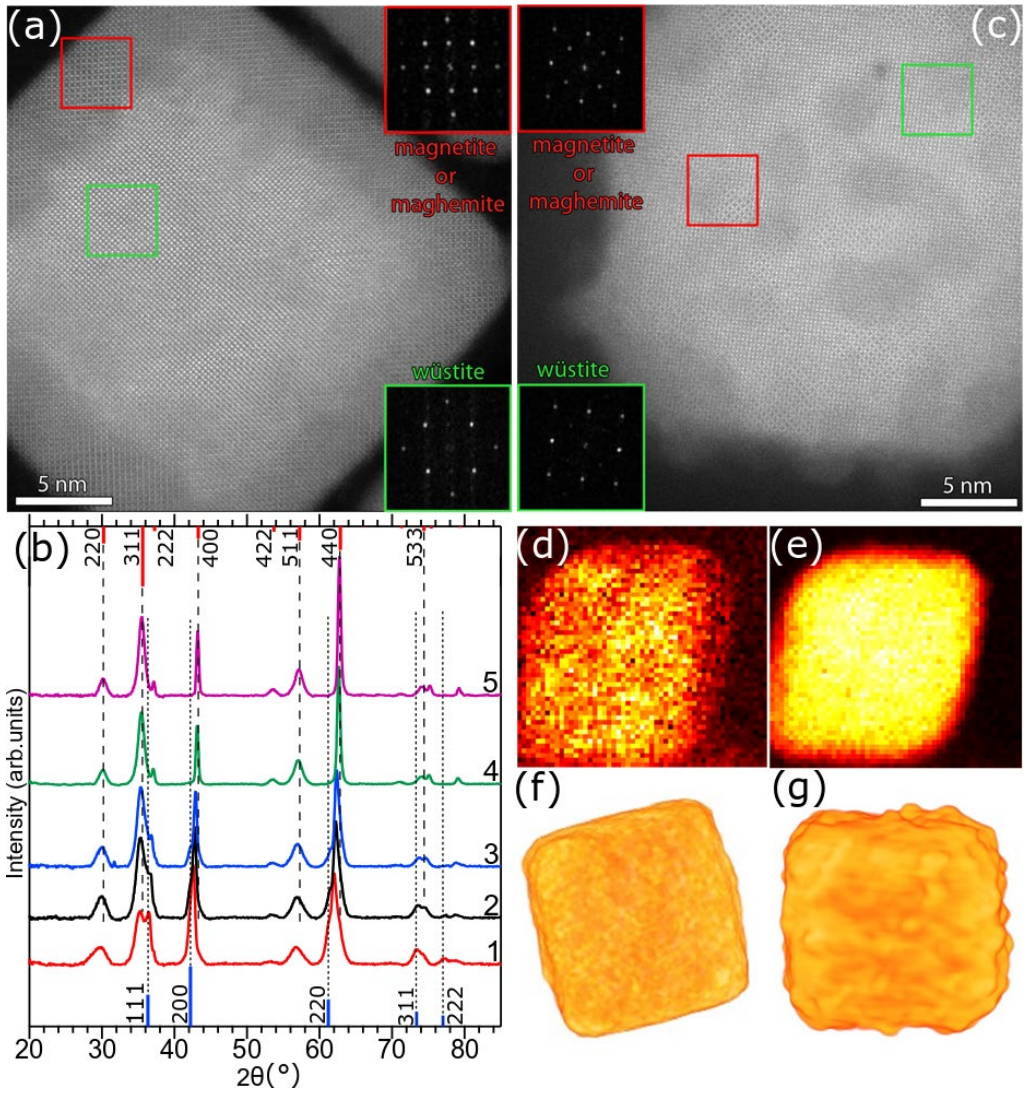

Figure 3. (a) High resolution HAADF-STEM image of as-prepared (IO23/0) particles: insets are Fourier analysis diffraction patterns of regions containing FeO and magnetite/maghemite. (b) X-

ray diffraction patterns of all the samples: (1) IO23/0, (2) IO23/3, (3) IO23/6, (4) IO23/24, and (5) IO23/48. (c) High resolution HAADF-STEM image of the IO23/48 particles: insets are Fourier analysis diffraction patterns of regions containing FeO and magnetite/maghemite. (d) Fe^{+2} and (e) Fe^{+3} valency maps obtained by fitting the EELS spectra in each pixel to the reference spectra. (f) and (g) 3D visualizations of individual IO23/0 and IO23/48 nanocubes, respectively, which were reconstructed using electron tomography. Darker spots in the HAADF-STEM image (c) are due to a relatively long exposure time to the high energy electron beam.

^{57}Fe Mössbauer spectroscopy (MS) was performed in order to differentiate between the magnetite and maghemite phases[49] and to study the magnetization dynamics of the IO23/48 particles. The shape of the 300 K spectrum, having more weight to the outer lines at the positive velocity side, clearly indicates the presence of Fe_3O_4 (Figure 4a).[50,51] It was possible to fit all MS spectra with a superposition of three magnetic hyperfine patterns. Two 6-line patterns (#1 and #2) are dominant, showing a distribution (assumed Gaussian) of static magnetic hyperfine fields. A weaker third one (#3) is better approached assuming a relaxation pattern due to dynamical fluctuations of the hyperfine field, as it is expected for nanoparticles (refer to Table 2).

First, we concentrate on the contributions from the static patterns. Both the center shifts (S) and the relative spectral areas (RA) of the 300 K spectrum are well consistent with magnetite. Subspectra #1 and #2 correspond to the Fe^{3+} in the tetrahedral A sites and the $Fe^{2.5+}$ in the octahedral B sites due to the fast electron hopping between Fe^{2+} and Fe^{3+} at this temperature. The area ratio of RA (#1) and RA (#2) is 0.6(1) (the ideal one would be 0.5), indicating that there are Fe^{2+} deficiencies in octahedral sites. Upon lowering temperature the area ratio changes as the electron hopping slows down. This results in the presence of Fe^{3+} in both the A and B sites, and Fe^{2+} in the B sites. In bulk magnetite this is connected to a well-defined phase transition, the

Verwey transition, from cubic to monoclinic around 120 K.[52] Mössbauer spectra of magnetite nanoparticles with sizes comparable to ours have shown that the transition may occur continuously over a wide range of temperatures, caused by fractal-like granular assemblies originated from the synthesis.[51] At lower temperatures, even a well crystallized magnetite reveals a complex pattern due to the presence of Fe^{3+} (A), Fe^{2+} and Fe^{3+} in the distorted B sites. However, based on our MS spectra at 20 K, no distinctions can be made among the various octahedral sites. Despite this, subspectra #1 and #2 can be assigned to Fe^{3+} and Fe^{2+} with a spectral area ratio of 2.3(2) based on the center shifts. This diverges from the ideal ratio of 2 in magnetite, once more indicating that there are some Fe^{2+} deficiencies.

For all temperatures, we find an additional spectrum (#3) that is attributed to some trivalent iron ions, which are subjected to magnetic moment fluctuations. For the fitting, we have used a standard 2-level relaxation process without exchange splitting.[53] Moment fluctuation rates are in the order of 100 MHz. A close-lying origin of this contribution could be iron on the surface layers of particles. While the spectral area of #3 amounts to about 10% at low temperatures, it increases to about 30% of the total spectral area at 300 K. The increase is mainly due to approaching the superparamagnetic blocking temperature of the particles' ensemble. Furthermore, we have found no resolved spectral contribution of FeO, which typically shows two doublets with divalent isomer shifts of *ca.*1 mm/s[54] that should become clearly visible at 300 K (when FeO is in its paramagnetic state). Further discussions on the superparamagnetic behavior of the nanocubes can be found in the ESI.

A remarkable feature of zero-field-cooled (ZFC) curves is the appearance of a sharp Verwey transition hump upon annealing for 6 h (IO23/6) (Figure 4b and S11). The transition peak does not exist in the IO23/0 sample and becomes more pronounced from the IO23/3 sample to the IO23/6

sample. The transition occurs at *ca.* 120 K in these nanocubes, which perfectly matches the transition temperature of bulk Fe_3O_4, *i.e.* 121 K.[52] Noticeably, the Verwey hump disappears in the IO23/48 sample as if the transition happens over a wide temperature range, in agreement with the previous findings from Mössbauer spectroscopy.[51] This phenomenon could be related to some Fe^{2+} deficiencies, a short-range cation disorder, and a spin disorder. It is also known that off-stoichiometric magnetite nanoparticles do not reveal a sudden rise in M around the transition temperature.[29,52] The Fe^{2+} deficiencies, remaining FeO sub-domains, and structural defects distort the magnetic domain coherency and presumably results in the reduction of KV_m and H_A. These features drive the overall relaxation to the Néel rather than the Brownian. Temperature dependent AC susceptibility spectra recorded at different excitation frequencies reveal interesting features such as a pronounced χ'' kink at *ca.* 300 K (Figure 4c). This kink could be related to the blocking temperature T_B of the Fe_3O_4 domains, which are separated by tiny FeO domains and/or anti-phase boundaries. Moreover, there seems to be another χ'' peak at temperatures higher than 400 K, which can be attributed to an increase in the T_B due to inter-particle dipole-dipole interactions[55] and/or the collective behavior of the Fe_3O_4 domains within a single nanocube.

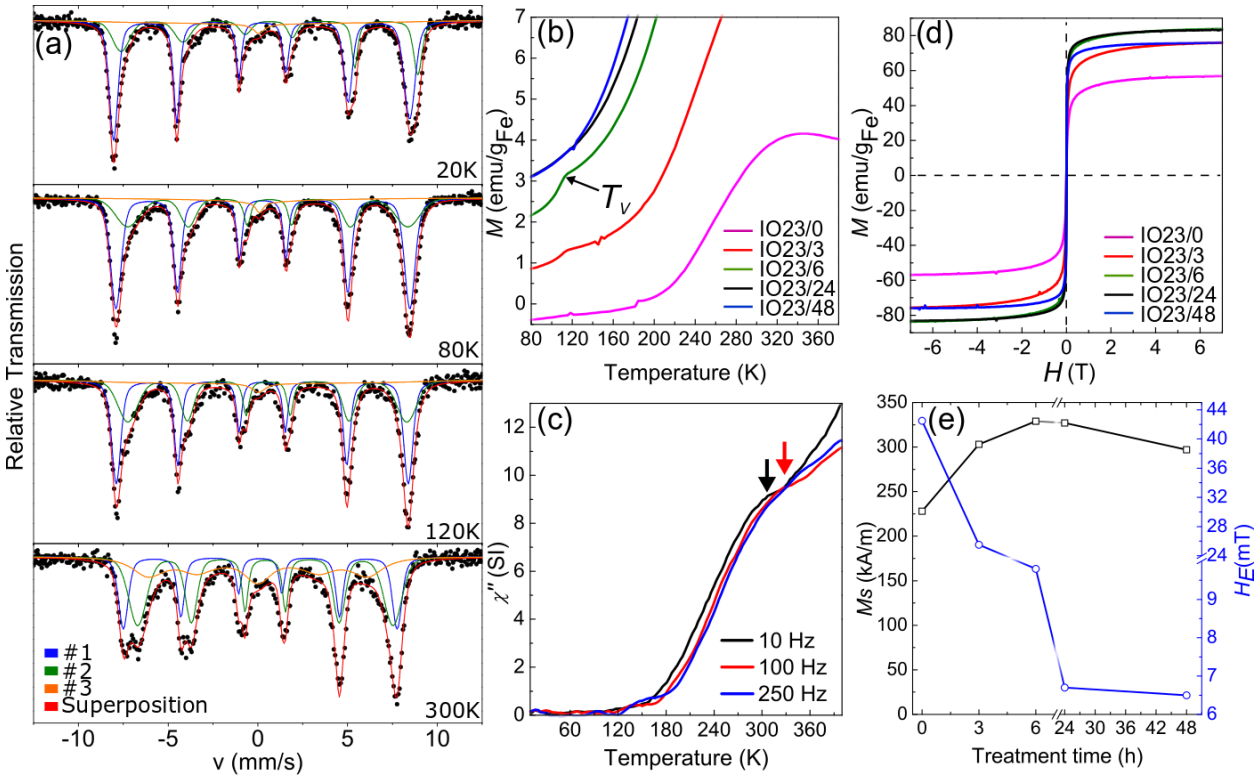

Figure 4. (a) ^{57}Fe Mössbauer absorption spectra of IO23/48 recorded at different temperatures. The red lines are the best fits to experimental data composed of a superposition of various subspectral components (#1, #2, #3). (b) Temperature dependent zero-field-cooled ZFC magnetization curves of IO23 sample series recorded at 5 mT warming-cooling fields. (c) Temperature dependent imaginary parts χ'' of the susceptibility measured at various excitation frequencies ω. (d) *M-H* loops recorded at 298 K, and (e) M_s values estimated from the fits to the *M-H* curves and the exchange bias fields H_E which were derived from FC hysteresis loops at 10 K.

Table 2: Hyperfine parameters of ^{57}the Fe Mössbauer spectra of the IO23/48 sample recorded at different temperatures.

T (K)	subspectrum	S (mm/s)	B (T)	σ (T)	RA(%)
20	#1	0.34(1)	51.3(2)	1.2(2)	62(2)
20	#2	0.74(1)	51.4(2)	1.7(2)	27(2)
20	#3	0.2(1)	50*		11(3)
80	#1	0.39(1)	50.9(2)	1.3(2)	61(2)
80	#2	0.71(1)	48.5(2)	3.7(2)	32(2)

80	#3	0.2(1)	50*		7(3)
120	#1	0.36(1)	50.6(2)	1.0(2)	51(2)
120	#2	0.66(1)	48.3(2)	2.9(2)	39(2)
120	#3	0.2(1)	50*		11(3)
300	#1	0.24(1)	47.4(2)	1.1(2)	27(2)
300	#2	0.52(1)	44.2(2)	2.6(2)	44(2)
300	#3	0.1(2)	40*		29(3)

T: absorber temperature; S: center shift relative to α-Fe at room temperature; B: magnetic hyperfine field; σ: width of Gaussian distribution of *B*; RA: relative spectral area contribution; *: fixed parameter, 2-level relaxation pattern (ref. to the main text)

The magnetization *M* increases abruptly during the initial stages of the thermal treatment (Figure 4d). The saturation magnetization M_s values were obtained by fitting *M-H* curves to a discrete form of the Langevin function (Eq. S12, ESI). Firstly, M_s increased from 225 to 325 kA/m during the first 24 h of the treatment then it dropped as the treatment was prolonged to 48 h (Figure 4e). As is the case for the ferrimagnetic Fe_3O_4, the overall magnetization originates from the uncompensated Fe^{2+} spins, therefore the reduced M_s of the IO23/48 can be presumably attributed to the Fe^{2+} deficiencies. Although it seems that M_s reaches an apex after 24 h treatment, the particle's magnetic moment *m* grows twice (from 5.3×10^{-19} A·m^2 to 1.1×10^{-18} A·m^2) upon 48 h treatment. This can be qualitatively discerned by observing that the normalized *M-H* curves reach the non-linear regime at lower magnetic fields (Figure S12). It is worth to mention that the intermediate IO23/6 nanocubes reveal the most bulk-like Fe_3O_4 inherent properties such as the highest *K* and M_s values among all the samples. The exchange bias field H_E, which was estimated from the FC hysteresis loops at 10 K (Figure S13), drops gradually over time which indicates a slow reduction in the volume of the AFM-FiM interface. It should be noted that H_E does drop to 6.5 mT in the IO23/48 sample. Structural defects such as anti-phase boundaries, spin canting, and tiny FeO sub-domains could be accounted for a non-zero H_E.

In order to elaborate on the viscosity and clustering independent heating response of the IO23/48 once exposed to the cellular environment or after cellular internalization we have designed two experiments. In the first one, the response of the SAR to a progressive internalization/association of the nanoparticles was evaluated. The nanoparticles (50 μL at 4 g_{Fe}/L) were added to a pellet of 5×10^6 ovarian cancer cells (IGROV-1 cell line), which simulate a small tumor mass, and the calorimetric SAR measurements were carried out at set incubation periods (0, 15, 45, 90 and 180 minutes). The heat profile and estimated SAR values indicate that there was no drop in the particles' heating efficiency within the first 180 minutes, albeit a 30% of the initial nanoparticle dose (0.06mg of iron) was found associated to the cell pellet (Figure. 5b and Figure S14(a)). This suggests that the heating capability of the IO23/48 nanocubes remains unchanged when progressively associated or internalized by the cells (see TEM images of the nanoparticles internalization, Figure S15(a)). This significantly differs from what has been reported for viscosity-dependent iron oxide nanocubes or nanospheres of similar sizes when incubated with tumor cells in similar cellular conditions.[37]

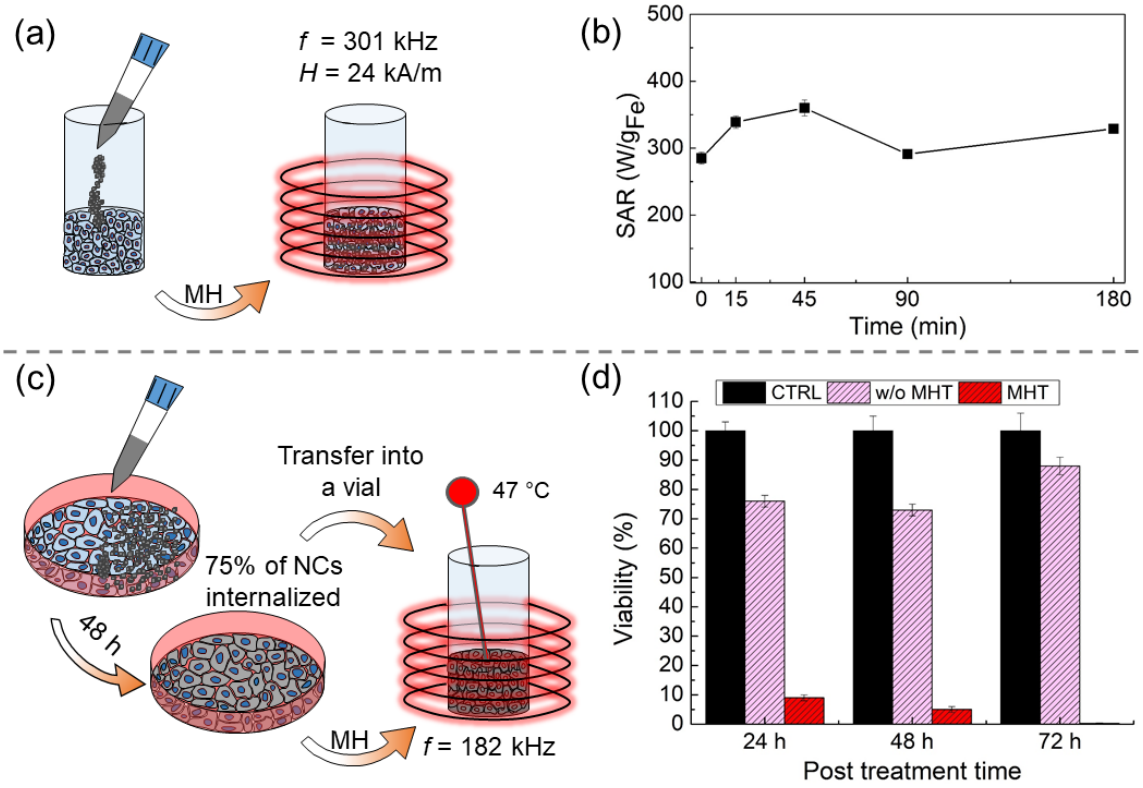

Figure 5. (a) Scheme of the adopted strategy for evaluating the heating performance of the IO23/48 particles once interacting with IGROV-1 cell pellet. (b) SAR values measured at field frequency and amplitude of 301 kHz and 24 kA/m at different incubation time intervals. (c) Scheme of the intracellular hyperthermia experiment on the IGROV-1 cell pellet and the nanocubes after 48 h of incubation. (d) PrestoBlue viability assays on the cells re-cultured for 24, 48 and 72 h, which were treated with MHT (red bar) and without (w/o) MHT (pink bar). The viability of the treated cells was normalized to control cells (black bar, no nanoparticles and no MHT exposure).

In the second experiment, the suitability of the IO23/48 particles, upon the cellular internalization, to induce temperature raise and cellular damage was probed. For this aim, adherent IGROV-1 cells were incubated with the IO23/48 nanocubes (50 µL at 8 g_{Fe}/L in 2 mL of medium) for 48 h to ensure an efficient particle uptake. It was found that a 75% of the administered nanoparticle dose (0.3 mg of iron) was internalized or associated to the cell pellet, as evidenced by TEM studies

(Figure S15(b)). The magnetic hyperthermia treatment (MHT) was performed on the cell pellet at the frequency of 182 kHz and field amplitude, which was varied from 40 kA/m at the beginning of the treatment to approximately 28 kA/m once the desired temperature of 47°C was reached (Figure S14(b)). Remarkably, the cell pellet was able to maintain this temperature for 90 minutes. The cytotoxicity PrestoBlue assay, on the cells once re-cultured for 24, 48 and 72 h, shows that the viability of cells that were exposed to MHT was severely compromised (red bar, Figure 5d), while a modest toxicity was exhibited by the cells that were non-exposed to MHT (pink bar, Figure 5d). The intracellular organization and typical cytosolic and nuclear structures of the cells appear to collapse completely after the MHT (Figure S15(c)-(d)). These data indicate that the IO23/48 particles are highly-efficient hyperthermia mediators as they are able to supply a required thermal stress to the cells in order to induce their death under biologically safe field conditions.

In summary, we have shown that it is not necessary to have stoichiometric and defect-free iron oxide nanoparticles in order to design efficient magnetic nanoparticles for intracellular magnetic hyperthermia. On the contrary, we have demonstrated here that one can turn cation deficiencies and structural defects into positive features that enhance the heating. We have identified that the FeO-Fe_3O_4 CS nanocubes transform into the Fe^{2+} deficient Fe_3O_4 nanocubes with structural defects *e.g.* anti-phase boundaries and tiny FeO sub-domains, as was revealed by HADDF-STEM, EELS, and ^{57}Fe Mössbauer analyses, after 48 h of thermal treatment at 80°C in water. Not only did their magnetic losses (SAR value) increase significantly throughout the process, but the treated nanocubes also exhibit an exceptionally stable SAR regardless of the medium viscosity, aggregation as well as association and internalization to the IGROV-1 cells. The same features have not yet been reported for similarly sized single phase magnetite nanocubes, as they relax via the Brownian process and thus responding dramatically to such environmental stimuli. The

nanocubes treated for 48 h have the largest SAR that has been reported thus far for iron oxide nanoparticles in such an environment. We have identified that the survival and migration of the FeO sub-domains, which are randomly distributed throughout the entire particle, are caused by the high pressure exerted by the growing Fe_3O_4 domains. It is plausible that the Fe^{2+} deficiencies and structural defects break the long-range magnetic ordering in the magnetite phase, resulting in reduced H_A and KV_m quantities. These features together with spin canting seem to account for the domination of the Néel relaxation in the IO23/48 nanocubes, which is not a general feature of particles with large magnetic losses at moderate field conditions (*i.e.* 182 kHz and 28 kA/m). These features favor the preservation of magnetic losses into intracellular environments.

Last but not least, the non-interactive nature and colloidal stability of the freshly prepared CS nanocubes make them very attractive in terms of conducting a particle water phase transfer using any type of water transfer protocol instead of highly interacting single phase magnetic nanocubes (especially those with edge lengths above 20 nm). The processed nanocubes possess a remarkably small anisotropy field H_A given their comparatively small K. Therefore, they would require a relatively low excitation magnetic field in order to go through the major hysteresis loop wherein their full heating capacity will be harnessed. Given that *in-vivo* magnetic particle imaging (MPI) and intracellular magnetic hyperthermia share similar physics of magnetism wherein optimal nanoparticles should relax *via* the Néel mechanism, the engineered 23 nm are potential theranostic agents for combined MPI/MH intracellular assays.

ASSOCIATED CONTENT

Supporting Information

Materials, syntheses, characterization methods, data analyses, numerical simulations, and Figures S1-S15 are presented.

AUTHOR INFORMATION

Corresponding Authors

Teresa Pellegrino: Teresa.pellegrino@iit.it

Aidin Lak: aidinlak@gmail.com, Lak.Aidin@physik.uni-muenchen.de

Present Address

Aidin Lak: Department of Physics, Nanosystem Initiative Munich and Center for Nanoscience, LMU Munich, Amalienstr. 54, 80799 Munich, Germany.

David Cabrera: Institute for Science and Technology in Medicine, Keele University, Guy Hilton Research Centre, Thornburrow Drive, Hartshill, Stoke-on-Trent ST4 7QB, United Kingdom.

Author Contributions

A.L. and T.P. devised the research. A.L. performed the particle synthesis experiments. A.L. and M.C. conducted the calorimetric hyperthermia measurements. T.B.M. designed and synthesized the polymeric ligands. A.L. and T.B.M. carried out the particle water transfer and DLS analyses. A.L and H.R. performed the ACS measurements. A.L. analyzed and modeled the ACS results. F. L. gave insight into the interpretation and modeling of the ACS spectra. D.C., L.M., and F.J.T. carried out dynamic hysteresis measurements and data analyses. F.J.L. and E.S. carried out

Mössbauer measurements and modeling. F.J.L. and E.S. wrote the Mössbauer section of the manuscript. N.W. and S.B. performed HAADF-STEM and EELS measurements and analyses, and wrote the related sections. L.M. gave insight into the structural and crystallographic features of the particles. A.L. performed all SQUID measurements, analyses, and modeling. S.F. conducted AC mode SQUID measurements. S.M. and A.L. performed the XRD measurements. A.L. analyzed and modeled the XRD patterns. M.C. performed the cellular hyperthermia experiments and wrote the related sections. M.C. performed TEM studies on the cells. A.L. and T.P. wrote the manuscript. All authors have given approval to the final version of the manuscript.

Notes

The authors declare no competing financial interest.

ACKNOWLEDGMENT

This work is partially funded by the European Research Council (starting grant ICARO, Contract No. 678109 and COLOURATOM-335078), Spanish Ministry of Economy and Competitiveness (MAT2016-81955-REDT, SEV-2016-0686, MAT2017-85617-R) Comunidad de Madrid (NANOFRONTMAG-CM, S2013/MIT-2850), the European COST Action TD1402 (RADIOMAG), and Ramon y Cajal subprogram (RYC-2011-09617). Financial support from the Deutsche Forschungsgemeinschaft, DFG Priority Program 1681 (LU800/4-3). S.B. and N.W. acknowledge financial support from the Research Foundation Flanders (FWO, Belgium) through Project funding G038116N. A.L. acknowledges the Alexander von Humboldt Foundation for the Postdoctoral Research Fellow funding. Mr Emilio J. Artés from the Advanced Instrumentation Unit (iMdea Nanociencia) is acknowledged for his technical assistance. L. M acknowledges the predoctoral fellowship funded from Comunidad de Madrid (PEJD-2017-PRE/IND-4189). Authors thank Tiziano Catelani and Doriana Debellis for the preparation of TEM cell samples.

REFERENCES

(1) Lee, N.; Choi, Y.; Lee, Y.; Park, M.; Moon, W. K.; Choi, S. H.; Hyeon, T. Water-Dispersible Ferrimagnetic Iron Oxide Nanocubes with Extremely High R2 Relaxivity for Highly Sensitive in Vivo MRI of Tumors. *Nano Lett.* **2012**, *12*, 3127–3131.

(2) Guardia, P.; Di Corato, R.; Lartigue, L.; Wilhelm, C.; Espinosa, A.; Garcia-Hernandez, M.; Gazeau, F.; Manna, L.; Pellegrino, T. Water-Soluble Iron Oxide Nanocubes with High Values of Specific Absorption Rate for Cancer Cell Hyperthermia Treatment. *ACS Nano* **2012**, *6*, 3080–3091.

(3) Gleich, B.; Weizenecker, J. Tomographic Imaging Using the Nonlinear Response of Magnetic Particles. *Nature* **2005**, *435*, 1214.

(4) Bauer, L. M.; Situ, S. F.; Griswold, M. A.; Samia, A. C. S. High-Performance Iron Oxide Nanoparticles for Magnetic Particle Imaging-Guided Hyperthermia (HMPI). *Nanoscale* **2016**, *8*, 12162–12169.

(5) Périgo, E. A.; Hemery, G.; Sandre, O.; Ortega, D.; Garaio, E.; Plazaola, F.; Teran, F. J. Fundamentals and Advances in Magnetic Hyperthermia. *Appl. Phys. Rev.* **2015**, *2* (4).

(6) Maier-Hauff, K.; Ulrich, F.; Nestler, D.; Niehoff, H.; Wust, P.; Thiesen, B.; Orawa, H.; Budach, V.; Jordan, A. Efficacy and Safety of Intratumoral Thermotherapy Using Magnetic Iron-Oxide Nanoparticles Combined with External Beam Radiotherapy on Patients with Recurrent Glioblastoma Multiforme. *J. Neurooncol.* **2011**, *103*, 317–324.

(7) Kolosnjaj-Tabi, J.; Lartigue, L.; Javed, Y.; Luciani, N.; Pellegrino, T.; Wilhelm, C.; Alloyeau, D.; Gazeau, F. Biotransformations of Magnetic Nanoparticles in the Body. *Nano Today* **2016**, *11*, 280–284.

(8) Park, J.; An, K.; Hwang, Y.; Park, J.-G.; Noh, H.-J.; Kim, J.-Y.; Park, J.-H.; Hwang, N.-M.;

Hyeon, T. Ultra-Large-Scale Syntheses of Monodisperse Nanocrystals. *Nat. Mater.* **2004**, *3*, 891–895.

(9) Bronstein, L. M.; Atkinson, J. E.; Malyutin, A. G.; Kidwai, F.; Stein, B. D.; Morgan, D. G.; Perry, J. M.; Karty, J. a. Nanoparticles by Decomposition of Long Chain Iron Carboxylates: From Spheres to Stars and Cubes. *Langmuir* **2011**, *27*, 3044–3050.

(10) Bronstein, L.; Huang, X.; Retrum, J.; Schmucker, A.; Pink, M.; Stein, B. D.; Dragnea, B. Influence of Iron Oleate Complex Structure on Iron Oxide Nanoparticle Formation. *Chem. Mater.* **2007**, *19*, 3624–3632.

(11) Walter, A.; Billotey, C.; Garofalo, A.; Ulhaq-Bouillet, C.; Lefevre, C.; Taleb, J.; Laurent, S.; Elst, L. Vander; Muller, R. N.; Lartigue, L.; et al. Mastering the Shape and Composition of Dendronized Iron Oxide Nanoparticles to Tailor Magnetic Resonance Imaging and Hyperthermia. *Chem. Mater.* **2014**, *26*, 5252–5264.

(12) Lee, N.; Kim, H.; Choi, S. H.; Park, M.; Kim, D.; Kim, H.-C.; Choi, Y.; Lin, S.; Kim, B. H.; Jung, H. S.; et al. Magnetosome-like Ferrimagnetic Iron Oxide Nanocubes for Highly Sensitive MRI of Single Cells and Transplanted Pancreatic Islets. *Proc. Natl. Acad. Sci. U. S. A.* **2011**, *108*, 2662–2667.

(13) Kovalenko, M. V; Bodnarchuk, M. I.; Lechner, R. T.; Hesser, G.; Schäffler, F.; Heiss, W. Fatty Acid Salts as Stabilizers in Size-and Shape-Controlled Nanocrystal Synthesis: The Case of Inverse Spinel Iron Oxide. *J. Am. Chem. Soc.* **2007**, *129*, 6352–6353.

(14) Shavel, A.; Rodri, B.; Pacifico, J.; Spasova, M.; Farle, M.; Liz-marza, L. M.; Rodrı, B. Shape Control in Iron Oxide Nanocrystal Synthesis , Induced by Trioctylammonium Ions. *Chem. Mater.* **2009**, *21*, 5843–5849.

(15) Zhou, Z.; Zhu, X.; Wu, D.; Chen, Q.; Huang, D.; Sun, C.; Xin, J.; Ni, K.; Gao, J. Anisotropic

Shaped Iron Oxide Nanostructures: Controlled Synthesis and Proton Relaxation Shortening Effects. *Chem. Mater.* **2015**, *27*, 3505–3515.

(16) Noh, S. H.; Na, W.; Jang, J. T.; Lee, J. H.; Lee, E. J.; Moon, S. H.; Lim, Y.; Shin, J. S.; Cheon, J. Nanoscale Magnetism Control via Surface and Exchange Anisotropy for Optimized Ferrimagnetic Hysteresis. *Nano Lett.* **2012**, *12*, 3716–3721.

(17) Pichon, B. P.; Gerber, O.; Lefevre, C.; Florea, I.; Fleutot, S.; Baaziz, W.; Pauly, M.; Ohlmann, M.; Ulhaq, C.; Ersen, O.; et al. Microstructural and Magnetic Investigations of Wüstite-Spinel Core-Shell Cubic-Shaped Nanoparticles. *Chem. Mater.* **2011**, *23*, 2886–2900.

(18) Lak, A.; Ludwig, F.; Scholtyssek, J. M.; Dieckhoff, J.; Fiege, K.; Schilling, M. Size Distribution and Magnetization Optimization of Single-Core Iron Oxide Nanoparticles by Exploiting Design of Experiment Methodology. *IEEE Trans. Magn.* **2013**, *49*, 201–207.

(19) Sun, X.; Huls, N. F.; Sigdel, A.; Sun, S. Tuning Exchange Bias in Core/Shell FeO/Fe_3O_4 Nanoparticles. *Nano Lett.* **2012**, *12*, 246–251.

(20) Wetterskog, E.; Tai, C. W.; Grins, J.; Bergström, L.; Salazar-Alvarez, G. Anomalous Magnetic Properties of Nanoparticles Arising from Defect Structures: Topotaxial Oxidation of $Fe_{1-x}O|Fe_{3-\Delta}O_4$ Core|shell Nanocubes to Single-Phase Particles. *ACS Nano* **2013**, *7*, 7132–7144.

(21) Lak, A.; Kraken, M.; Ludwig, F.; Kornowski, A.; Eberbeck, D.; Sievers, S.; Litterst, F. J.; Weller, H.; Schilling, M. Size Dependent Structural and Magnetic Properties of $FeO-Fe_3O_4$ Nanoparticles. *Nanoscale* **2013**, *5*, 12286–12295.

(22) Palchoudhury, S.; An, W.; Xu, Y.; Qin, Y.; Zhang, Z.; Chopra, N.; Holler, R. A.; Turner, C. H.; Bao, Y. Synthesis and Growth Mechanism of Iron Oxide Nanowhiskers. *Nano Lett.*

2011, *11*, 1141–1146.

(23) Hai, H. T.; Yang, H. T.; Kura, H.; Hasegawa, D.; Ogata, Y.; Takahashi, M.; Ogawa, T. Size Control and Characterization of Wustite (Core)/Spinel (Shell) Nanocubes Obtained by Decomposition of Iron Oleate Complex. *J. Colloid Interface Sci.* **2010**, *346*, 37–42.

(24) Estrader, M.; López-Ortega, A.; Golosovsky, I. V.; Estradé, S.; Roca, A. G.; Salazar-Alvarez, G.; López-Conesa, L.; Tobia, D.; Winkler, E.; Ardisson, J. D.; et al. Origin of the Large Dispersion of Magnetic Properties in Nanostructured Oxides: Fe_xO/Fe_3O_4 Nanoparticles as a Case Study. *Nanoscale* **2015**, *7*, 3002–3015.

(25) Torruella, P.; Arenal, R.; De La Peña, F.; Saghi, Z.; Yedra, L.; Eljarrat, A.; López-Conesa, L.; Estrader, M.; López-Ortega, A.; Salazar-Alvarez, G.; et al. 3D Visualization of the Iron Oxidation State in FeO/Fe_3O_4 Core-Shell Nanocubes from Electron Energy Loss Tomography. *Nano Lett.* **2016**, *16* (8), 5068–5073.

(26) Redl, F. X.; Black, C. T.; Papaefthymiou, G. C.; Sandstrom, R. L.; Yin, M.; Zeng, H.; Murray, C. B.; O'Brien, S. P. Magnetic, Electronic, and Structural Characterization of Nonstoichiometric Iron Oxides at the Nanoscale. *J. Am. Chem. Soc.* **2004**, *126*, 14583–14599.

(27) Guardia, P.; Perez-Juste, J.; Labarta, A.; Batlle, X.; Liz-Marzan, L. M. Heating Rate Influence on the Synthesis of Iron Oxide Nanoparticles: The Case of Decanoic Acid. *Chem. Commun.* **2010**, *46*, 6108–6110.

(28) Kim, D.; Lee, N.; Park, M.; Kim, B. H.; An, K.; Hyeon, T. Synthesis of Uniform Ferrimagnetic Magnetite Nanocubes. *J. Am. Chem. Soc.* **2009**, 454–455.

(29) Chen, R.; Christiansen, M. G.; Sourakov, A.; Mohr, A.; Matsumoto, Y.; Okada, S.; Jasanoff, A.; Anikeeva, P. High-Performance Ferrite Nanoparticles through Nonaqueous Redox

Phase Tuning. *Nano Lett.* **2016**, *16*, 1345–1351.

(30) Unni, M.; Uhl, A. M.; Savliwala, S.; Savitzky, B. H.; Dhavalikar, R.; Garraud, N.; Arnold, D. P.; Kourkoutis, L. F.; Andrew, J. S.; Rinaldi, C. Thermal Decomposition Synthesis of Iron Oxide Nanoparticles with Diminished Magnetic Dead Layer by Controlled Addition of Oxygen. *ACS Nano* **2017**, *11*, 2284–2303.

(31) Hufschmid, R.; Arami, H.; Ferguson, R. M.; Gonzales, M.; Teeman, E.; Brush, L. N.; Browning, N. D.; Krishnan, K. M. Synthesis of Phase-Pure and Monodisperse Iron Oxide Nanoparticles by Thermal Decomposition. *Nanoscale* **2015**, *7*, 11142–11154.

(32) Nedelkoski, Z.; Kepaptsoglou, D.; Lari, L.; Wen, T.; Booth, R. A.; Oberdick, S. D.; Galindo, P. L.; Ramasse, Q. M.; Evans, R. F. L.; Majetich, S.; et al. Origin of Reduced Magnetization and Domain Formation in Small Magnetite Nanoparticles. *Sci. Rep.* **2017**, *7*, 45997.

(33) Kuimova, M. K.; Yahioglu, G.; Levitt, J. A.; Suhling, K. Molecular Rotor Measures Viscosity of Live Cells via Fluorescence Lifetime Imaging. *J. Am. Chem. Soc.* **2008**, *50*, 1–7.

(34) Cabrera, D.; Coene, A.; Leliaert, J.; Artés-Ibáñez, E. J.; Dupré, L.; Telling, N. D.; Teran, F. J. Dynamical Magnetic Response of Iron Oxide Nanoparticles Inside Live Cells. *ACS Nano* **2018**, *12*, 2741–2752.

(35) Fortin, J.-P.; Wilhelm, C.; Servais, J.; Ménager, C.; Bacri, J.-C.; Gazeau, F. Size-Sorted Anionic Iron Oxide Nanomagnets as Colloidal Mediators for Magnetic Hyperthermia. *J. Am. Chem. Soc.* **2007**, *129*, 2628–2635.

(36) Fortin, J. P.; Gazeau, F.; Wilhelm, C. Intracellular Heating of Living Cells through Néel Relaxation of Magnetic Nanoparticles. *Eur. Biophys. J.* **2008**, *37*, 223–228.

(37) Di Corato, R.; Espinosa, A.; Lartigue, L.; Tharaud, M.; Chat, S.; Pellegrino, T.; Ménager,

C.; Gazeau, F.; Wilhelm, C. Magnetic Hyperthermia Efficiency in the Cellular Environment Fordifferent Nanoparticle Designs. *Biomaterials* **2014**, *35*, 6400–6411.

(38) Sanz, B.; Calatayud, M. P.; De Biasi, E.; Lima, E.; Mansilla, M. V.; Zysler, R. D.; Ibarra, M. R.; Goya, G. F. In Silico before in Vivo: How to Predict the Heating Efficiency of Magnetic Nanoparticles within the Intracellular Space. *Sci. Rep.* **2016**, *6*, 1–10.

(39) Cabrera, D.; Lak, A.; Yoshida, T.; Materia, M. E.; Ortega, D.; Ludwig, F.; Guardia, P.; Sathya, A.; Pellegrino, T.; Teran, F. J. Unraveling Viscosity Effects on the Hysteresis Losses of Magnetic Nanocubes. *Nanoscale* **2017**, *9*, 5094–5101.

(40) Carrey, J.; Mehdaoui, B.; Respaud, M. Simple Models for Dynamic Hysteresis Loop Calculations of Magnetic Single-Domain Nanoparticles: Application to Magnetic Hyperthermia Optimization. *J. Appl. Phys.* **2011**, *109*, 083921.

(41) Usov, N. A.; Liubimov, B. Y. Dynamics of Magnetic Nanoparticle in a Viscous Liquid: Application to Magnetic Nanoparticle Hyperthermia. *J. Appl. Phys.* **2012**, *112* (2).

(42) Jordan, A.; Scholz, R.; Maier-Hauff, K.; van Landeghem, F. K. H.; Waldoefner, N.; Teichgraeber, U.; Pinkernelle, J.; Bruhn, H.; Neumann, F.; Thiesen, B.; et al. The Effect of Thermotherapy Using Magnetic Nanoparticles on Rat Malignant Glioma. *J. Neurooncol.* **2006**, *78*, 7–14.

(43) Guardia, P.; Riedinger, A.; Nitti, S.; Pugliese, G.; Marras, S.; Genovese, A.; Materia, M. E.; Lefevre, C.; Manna, L.; Pellegrino, T. One Pot Synthesis of Monodisperse Water Soluble Iron Oxide Nanocrystals with High Values of the Specific Absorption Rate. *J. Mater. Chem. B* **2014**, *2*, 4426–4434.

(44) Tay, Z. W.; Chandrasekharan, P.; Chiu-Lam, A.; Hensley, D. W.; Dhavalikar, R.; Zhou, X. Y.; Yu, E. Y.; Goodwill, P. W.; Zheng, B.; Rinaldi, C.; et al. Magnetic Particle Imaging

Guided Heating In Vivo Using Gradient Fields For Arbitrary Localization of Magnetic Hyperthermia Therapy. *ACS Nano* **2018**, *12*, 3699–3713.

(45) Mehdaoui, B.; Carrey, J.; Stadler, M.; Cornejo, A.; Nayral, C.; Delpech, F.; Chaudret, B.; Respaud, M. Influence of a Transverse Static Magnetic Field on the Magnetic Hyperthermia Properties and High-Frequency Hysteresis Loops of Ferromagnetic FeCo Nanoparticles. *Appl. Phys. Lett.* **2012**, *100*, 2010–2013.

(46) Ovejero, J. G.; Cabrera, D.; Carrey, J.; Valdivielso, T.; Salas, G.; Teran, F. J. Effects of Inter- and Intra-Aggregate Magnetic Dipolar Interactions on the Magnetic Heating Efficiency of Iron Oxide Nanoparticles. *Phys. Chem. Chem. Phys.* **2016**, *18*, 10954–10963.

(47) Lak, A.; Niculaes, D.; Anyfantis, G. C.; Bertoni, G.; Barthel, M. J.; Marras, S.; Cassani, M.; Nitti, S.; Athanassiou, A.; Giannini, C.; et al. Facile Transformation of FeO/Fe_3O_4 Core-Shell Nanocubes to Fe3O4 via Magnetic Stimulation. *Sci. Rep.* **2016**, *6*, 1–12.

(48) López-Ortega, A.; Lottini, E.; Bertoni, G.; De Julián Fernández, C.; Sangregorio, C. Topotaxial Phase Transformation in Cobalt Doped Iron Oxide Core/Shell Hard Magnetic Nanoparticles. *Chem. Mater.* **2017**, *29*, 1279–1289.

(49) Fock, J.; Bogart, L. K.; González-Alonso, D.; Espeso, J. I.; Hansen, M. F.; Varón, M.; Frandsen, C.; Pankhurst, Q. A. On the 'Centre of Gravity' Method for Measuring the Composition of Magnetite/Maghemite Mixtures, or the Stoichiometry of Magnetite-Maghemite Solid Solutions, via ^{57}Fe Mössbauer Spectroscopy. *J. Phys. D. Appl. Phys.* **2017**, *50*, 265005.

(50) Häggström, L.; Annersten, H.; Ericsson, T.; Wäppling, R.; Karner, W.; Bjarman, S. Magnetic Dipolar and Electric Quadrupolar Effects on the Mössbauer Spectra of Magnetite above the Verwey Transition. *Hyperfine Interact.* **1978**, *5*, 201–214.

(51) Dézsi, I.; Fetzer, C.; Gombkötő, Á.; Szűcs, I.; Gubicza, J.; Ungár, T. Phase Transition in Nanomagnetite. *J. Appl. Phys.* **2008**, *103*, 1–5.

(52) Lee, J.; Kwon, S. G.; Park, J.-G.; Hyeon, T. Size Dependence of Metal–Insulator Transition in Stoichiometric Fe_3O_4 Nanocrystals. *Nano Lett.* **2015**, *15*, 4337–4342.

(53) Blume, M.; Tjon, D. J. a. Mössbauer Spectra in a Fluctuating Environment. *Phys. Rev.* **1968**, *165*, 446–456.

(54) Eggert, A.; Riedel, E. Distribution and Valence of the Cations in Spinel Systems with Iron and Chromium, I The Formation of $FeCr_2O_4$ from Fe, Fe_2O_3 and Cr_2O_3 in Vacuum. *Z. Naturforsch.* **1990**, *45b*, 1522–1528.

(55) Bender, P.; Fock, J.; Frandsen, C.; Hansen, M. F.; Balceris, C.; Ludwig, F.; Posth, O.; Wetterskog, E.; Bogart, L. K.; Southern, P.; et al. Relating Magnetic Properties and High Hyperthermia Performance of Iron Oxide Nanoflowers. *J. Phys. Chem. C* **2018**, *122*, 3068–3077.

Supplementary Information

Designing Fe_3O_4 Nanocubes for Intracellular Magnetic Hyperthermia: Unraveling the Role of Fe^{2+} Deficiencies, FeO Sub-Domains, and Structural Defects

Aidin Lak,† Marco Cassani,† Binh T. Mai,† Naomi Winckelmans,‡ David Cabrera,§ Elaheh Sadrollahi,# Sergio Marras,† Hilke Remmer,‖ Sergio Fiorito,† Lucia Cremades-Jimeno,§ Fred Jochen Litterst,# Frank Ludwig,‖ Liberato Manna,† Francisco J. Teran,§,⊥ Sara Bals,‡ Teresa Pellegrino*†*

†Istituto Italiano di Tecnologia, via Morego 30, 16163 Genoa, Italy

‡EMAT, University of Antwerp, Groenenborgerlaan 171, B-2020 Antwerp, Belgium

§iMdea Nanociencia, Campus Universitario de Cantoblanco, 28049 Madrid, Spain

#Institute of Condensed Matter Physics, Technische Universität Braunschweig, Mendelssohn-Str. 3, 38106 Braunschweig, Germany

‖Institute for Electrical Measurement Science and Fundamental Electrical Engineering, Technische Universität Braunschweig, Hans-Sommer-Str. 66, 38106 Braunschweig, Germany

⊥Nanobiotecnología (iMdea Nanociencia), Unidad Asociada al Centro Nacional de Biotecnología (CSIC), 28049 Madrid, Spain

Materials and Methods

Materials:

Iron(III) chloride hexahydrate $FeCl_3.6H_2O$ (98%), 1-Octadecene (ODE, 90%), oleic acid (OLAC, 90%), triethylamine (TEA, 99%), and solvents with the highest purity grade were purchased from Sigma-Aldrich. N-tetracosane (99%) was purchased from Alfa Aesar. Sodium oleate (97%) was obtained from TCI. The chemicals were utilized without further purification.

Synthesis of the nanocubes:

The iron-oleate precursor was synthesized according to the procedure reported in Ref.,[1] with the only difference being that we did not use a vacuum to dry the iron-oleate.

To obtain 23 nm nanocubes, a mixture of 1.8 g (2 mmol) iron-oleate, 0.3 g sodium oleate (1 mmol), 0.282 g (1 mmol) oleic acid, 3.75 mL 1-Octadecene, and 5 g n-tetracosane was poured into a 50 mL three-neck glass flask, equipped with a thermometer and connected to a Schlenk line thorough a condenser. The mixture was degassed at 100 °C for 45 min in order to

remove volatile impurities. Afterwards, the flask was filled with N_2, heated up to 180 °C and kept for 20 min to dissolve the sodium oleate and obtain a fully homogeneous mixture. Subsequently, the mixture was heated up to 350 °C at a heating rate of 3 °C/min and soaked at this temperature for 30 min. After cooling the flask to 80 °C, the black viscous product was diluted and dissolved by adding 40 mL chloroform. The resultant particles were separated by adding a 1:2 v% mixture of methanol and acetone (anti-solvents) and centrifuging at 6000 rpm for 10 min. After each centrifugation step, the collected particles were re-dispersed in a 20 mL mixture (1:1 v%) of hexane and chloroform by vigorously shaking it. The procedure of adding anti-solvents and centrifugation was repeated five more times to obtain thoroughly clean particles. At the end of the washing step, the particles were dispersed in 40 mL of chloroform and stored at 4 °C for further use and characterization.

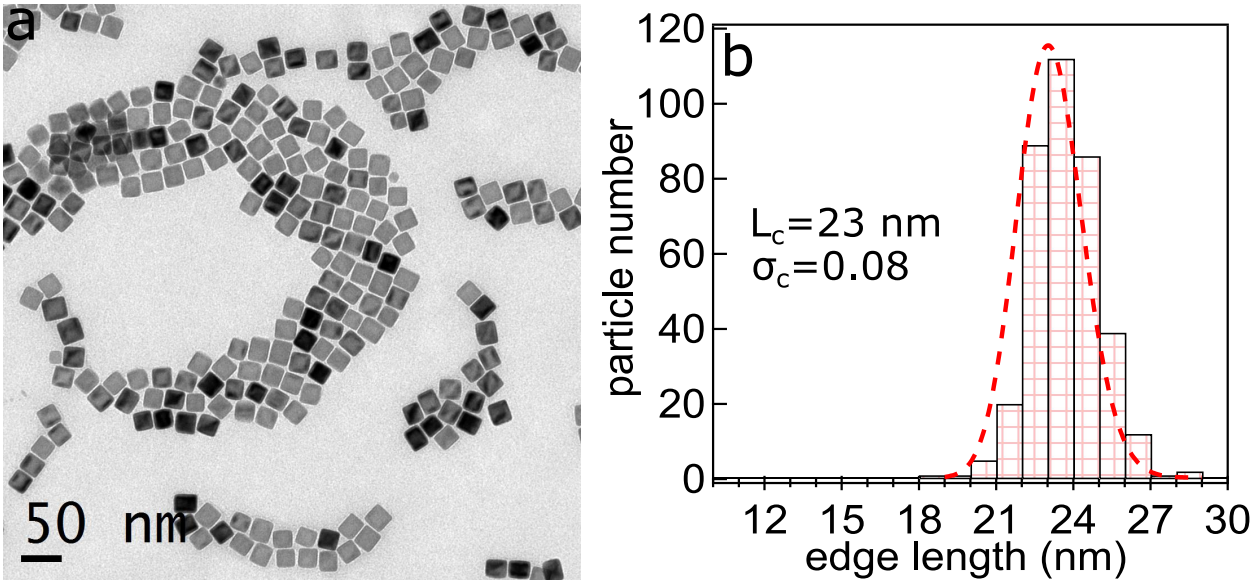

Figure S1. A typical TEM micrograph and particle size histogram of freshly synthesized 23 nm (IO23/0) FeO-Fe_3O_4 core-shell nanocubes.

Water transfer of the nanocubes:

The water transfer of the nanocubes was achieved using a block copolymer-based multi-dentate ligand which was synthesized using a two-step procedure based on photo-induced copper mediated radical polymerization according to a procedure set by some of our coauthors. Figure S2 shows the chemical structure of the block copolymer-based multi-dentate ligand that was used in this study, as well as its typical ^{1}H NMR spectrum.

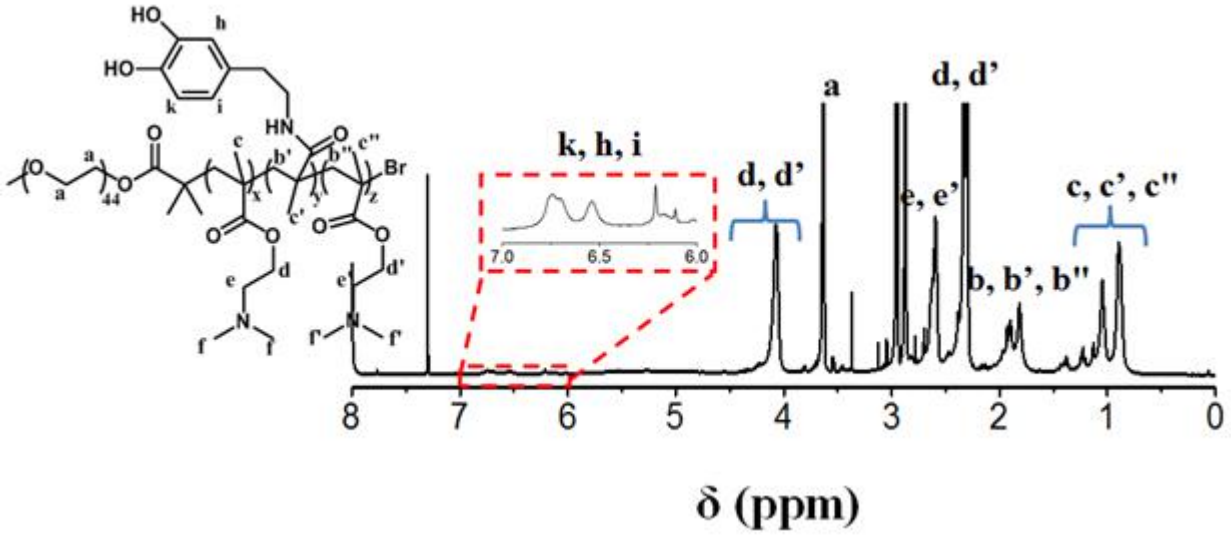

Figure S2. Chemical structure of block copolymer-based multi-dentate ligand and its ^{1}H NMR. The spectrum was recorded in $CDCl_3$ at 25^{o}C.

Thanks to the good solubility of the ligand in $CHCl_3$, we are able to set a simple and efficient water transfer protocol with an excellent yield in terms of particle recovery (*ca.* 90%). In a typical procedure, 10 mL of a nanocube suspension in chloroform (*i.e.* 20 mg of Fe) was mixed with 250 mg of block

copolymers, which had been dissolved in 10 mL chloroform and 1 mL TEA (10 v% of a polymer), in a 50 mL glass vial. The mixture was stirred rigorously overnight at room temperature (RT). Afterwards, three folds of hexane were added to the solution to precipitate the particles and dissolve and extract unwanted impurities. After centrifugation at 1000 rpm for 1 min, the particles were re-dispersed in 5 mL of tetrahydrofuran (THF), and a subsequent washing step was performed using hexane. Having precipitated the particles by centrifugation, the particles were thoroughly dried by purging N_2. The dried pellet like particles were dissolved in 10 mL of DI water *via* vigorous shaking. The particles were easily dispersed in water at this stage, indicating a successful ligand exchange with a good surface packing density. Next, the excessive amount of unbound polymers was removed by filter centrifugation (Amicon filter with 100 kDa molecular weight cut off) at 2500 rpm for 25 min. The cleaning process was repeated 5 times to ensure that the final particles are free of any unbound polymers. In the last run, the resultant particles were typically dispersed in 3-5 mL DI water to typically reach a $4g_{Fe}$/L iron concentration.

Stepwise oxidation of the nanocubes in an aqueous phase:

The nanocubes with an average edge length of 18 and 23 nm were gradually oxidized at 80°C after being transferred into water. Typically, 2 mL of aqueous particle suspensions at $4g_{Fe}$/L were poured into a 4 mL glass vial. The vial was tightly sealed and left in the oven at 80 °C for 3, 6, 24, 36, 48 h.

Induction of nanocube Clustering:

To induce particle clustering and thus increase the hydrodynamic size d_h, bovine serum albumin (BSA) solutions with different BSA contents (20 g/L and 50 g/L) were added to the IO23/48 particle dispersion, while the iron content was kept constant (2 g_{Fe}/L). After adding BSA, the dispersion was mixed by a vortex for 5 min and sonicated for 5 min. After incubating the dispersion for an hour at RT, it was sonicated for another 5 min prior to measuring the AC hysteresis loops and the hydrodynamic size by dynamic light scattering (DLS). The volume weighted DLS results of single and clustered nanocubes are summarized in Table S1.

Table S1. Intensity weighted d_h and PDI values extracted from DLS measurements on the clustered IO23/48 nanocubes.

notation	*BSA (mg/mL)*	*d_h (nm)*	*PDI*
Single NCs	0	74	0.20
Medium clusters	1.4	114	0.13
Large clusters	5.5	810	0.23

Characterization methods

Calorimetric measurement of the specific absorption rate (SAR). The calorimetric measurements to quantify the specific absorption rate (SAR) value of the nanocubes were conducted using a Nanoscale Biomagnetics (MN-nanoscale) instrument operating over a broad range of fields and

frequencies. The sample temperature was monitored using a fiber optic temperature probe. The sample's equilibrium temperature was reached every time prior to switching the magnetic field on. The SAR was calculated using the corrected slope method, given by

$$SAR = (C\frac{dT}{dt} + L\Delta T)/m_{np} \qquad \text{Eq. S1}$$

in which C is the dispersing medium heat capacity in J/K (C_{water}=4.185 1/mL), L is the linear-loss parameter in W/K, ΔT is the temperature difference between the sample and baseline (the solution temperature before switching off the field) and m_{np} is the total particle mass. This method provides accurate SAR values because it takes the heat dissipation from the medium to the environment into account.

Complex ac-susceptibility. **C**omplex ac-susceptibility (ACS) measurements were carried out using a setup operating from 200 Hz to 1 MHz at magnetic field amplitudes of $\mu_0 H_0$=95 µT. The ACS measurements were carried out at 295 K on 150 µL of nanoparticle dispersions in water (1 g_{Fe}/L) and various glycerol weight fractions (41.5 wt%, 72.8 wt% and 84.3 wt%, 2 g_{Fe}/L). For clarity, the spectrum of IO23/0 (Figure 2a) is multiplied by 4.2.

Field and temperature dependent magnetization measurements. Field dependent static magnetic measurements were carried out using a

Magnetic Property Measurement System (*MPMS-XL*, Quantum Design) with EverCool technology on immobile nanocubes. The immobile samples were prepared by mixing 50 µL of a nanocube water solution at an iron concentration of 1-2 g/L with 60 mg of gypsum in designated polycarbonate capsules and letting it dry thoroughly. The zero-field-cooled (ZFC) and field-cooled (FC) temperature dependent magnetization measurements were performed on samples prepared in the same way in the cooling field of 5 mT. The FC M-H hysteresis loops were recorded after the samples were cooled from RT to 10 K in 5 T magnetic fields. The residual magnetic field in the SQUID magnets was nulled using the designated low field Hall sensor prior to ZFC measurements. All the presented magnetization data are corrected with respect to the diamagnetic and paramagnetic contributions of water and gypsum using the automatic background subtraction routine. The curves were normalized to the iron concentration that was obtained from the elemental analysis.

^{57}Fe Mössbauer spectroscopy. ^{57}Fe Mössbauer absorption spectroscopy was performed on 23 nm particles that had been annealed for 48 h (IO23/48) using a standard spectrometer equipped with a He-flow cryostat to adjust the temperature. The sample mass corresponds to *ca.* 0.1 mg/cm^2 ^{57}Fe. The radiation source serves about 20 mCi of ^{57}Co in a Rhodium metal matrix which is kept at room temperature.

AC magnetometry. AC hysteresis loops were recorded with a home-made inductive magnetometer based on the one described by Connord et al[2],

operating at room temperature. The magnetic fields are generated by a Litz wire solenoid, inside which two counterwise-wounded compensated pick-up coils with the same diameter and number of turns collect the induction signal of the sample. Field frequencies and intensities are automatically tuned to 300 kHz and 24 kA/m. The equipment quantifies the magnetization from particles' aqueous dispersions, whose values are calibrated by comparing the magnetization values that were obtained under AC with quasi-static magnetic field conditions in a similar field intensity range. The AC magnetization signal was normalized to the iron mass.

Elemental analysis. The elemental analysis was performed using an Inductively Coupled Plasma-Atomic Emission Spectroscopy (ICP-AES) instrument (Thermo Fisher, iCap 6000). Typically, 10-50 µL of a nanocube suspension was digested in 1 mL of Aqua Regia in a volumetric flask. Afterwards, the flask was filled up to the graduation mark with Milli-Q water and filtered through 0.2 µm of membrane prior to the measurement.

Powder X-ray diffraction. Powder X-ray diffraction (XRD) analysis was conducted on a Rigaku Smart Lab diffractometer, equipped with a 9 kW CuK➔ rotating anode operating at 150 mA and 40 kV. The patterns were acquired in a Bragg-Brentano geometry over an angular range of 2⚠=20°-85°, using a D-teX Ultra 1D silicon strip detector set in X-ray fluorescence reduction mode. The samples were prepared by drop casting the concentrated particle suspensions on a zero diffraction silicon wafer.

Low-resolution Transmission electron microscopy (TEM). Low resolution TEM micrographs were taken using a JEOL JEM-1011 microscope operating at 100 kV. The samples were prepared by drying a drop of the diluted particle suspension on 400 mesh ultra-thin carbon coated TEM copper grids. The particle size distribution was analyzed using the automatic particle size analysis routine in ImageJ software on a low magnified TEM micrograph. Typically, more than 300 particles were taken into the analysis.

High-Resolution HAADF-STEM imaging. High resolution HAADF-STEM images were acquired using an aberration-corrected cubed FEI-Titan electron microscope at an operating voltage of 300 kV. A camera length of 115 mm was used to guarantee incoherent imaging of nanoparticles.

Electron tomography. The HAADF-STEM tilt series was acquired using a FEI Tecnai Osiris electron microscope operating at 200 kV. For the acquisition of the tilt series, a Fischione model 2020 singe tilt holder was used. The series was acquired using a tilt range from -76° to +76° with a tilt increment of 2°. The projection images were aligned using a cross-correlation algorithm together with a manual tilt axis adjustment which was implemented in the FEI Inspect3D software.[3] For the 3D reconstruction, the simultaneous iterative reconstruction technique (SIRT) was used as implemented in the ASTRA toolbox[4–6].

Electron energy loss spectroscopy (EELS). EELS experiments were performed using an aberration-corrected cubed FEI-Titan electron microscope operating at 120 kV.

Dynamic light scattering. The particle hydrodynamic size distribution was measured using a Malvern Zeta sizer operated in the 173° backscattered

mode on a highly diluted aqueous solution of nanocubes. The measurements were performed at 20 °C.

Cell culture. Ovarian cancer cells (IGROV-1, ATCC, UK) were cultured in RPMI-1640 medium (RPMI-1640, Merck, Kenilworth, USA) supplemented with 10% Fetal Bovine Serum (FBS), 1% Penicillin Streptomycin (PS) and 1% Glutamine at 37°C, 95% humidity with 5% CO_2. Cells were split every 3-4 days before reaching confluence.

Calorimetric measurement of the SAR on the cells. Magnetic hyperthermia studies on the cells incubated with nanoparticles were carried out using nanoScale DM1 Series (Biomagnetics Corp.). The SAR measurements on a mixture of cells and particles were performed at 301 kHz and 24 kA/m field conditions and 2 g_{Fe}/L. In detail, adherent IGROV-1 cells were detached with trypsin and counted using NucleoCounter® NC-100^{TM} (ChemoMetec, Denmark). Afterwards, 5×10^6 cells were resuspended in 50 µL of medium in small glass vial and subsequently 50 µL of the IO23/48 sample at 4 g_{Fe}/L were added to the vial. The SAR measurement, which typically take 2-3 minutes, was conducted at 0, 15, 45, 90 and 180 minutes after the incubation of the cells with the particles. The SAR value was determined by fitting the initial slope (i.e. first 20-30 seconds) of the temperature *vs.* time curve (Figure S14(b)) to a simplified version of the Eq. S1 without taking into account the loss to the medium L parameter. All the reported SAR values and error bars were calculated from the mean and standard deviation of at least three experimental measurements.

Elemental analysis of intracellular iron. The cell samples were digested according to a procedure already shown.[7] Briefly, 250 µL of a concentrated H_2O_2/HNO_3 (1:2) solution was added to the cells and then the mixture was kept for 3 h in water bath at 55 °C under sonication (in order to ensure the complete digestion of the cells components). After this step, which leads

to a complete evaporation of H_2O_2, a concentrated HCl was added (3:1 volume ratio with respect to HNO_3) to reach a final volume of 500 µL. The digestion proceeded over-night at RT. The solution was diluted to 5 mL with milliQ water and filtered with a PVDF filter (0.45 µm) before the analysis. The intracellular Fe concentration was measured by ICP-OES, Thermofisher ICAP 6300 duo).

TEM imaging of the cellular uptake. After the experiments, 800.000 IGROV-1 cells were collected, washed three times and resuspended in 500 µL of fresh medium. Afterwards, the same amount of growth medium supplemented with glutaraldeyde (2%) was added and the mixture was shacked for 45 min at RT. The cells were then centrifuged at 13.200 rpm for 10 min. The obtained pellet was then dissolved in Na-cacodylate buffer (0.1 M, pH 7.4) supplemented with glutaraldeyde (2%) and mixed for 1 h at RT. Afterwards, the cells were centrifuged at 14.000 rpm for 10 min. The washing in Na-cacodylate buffer (0.1 M) was repeated three times. Subsequently, the pellet was incubated with Na-cacodylate buffer (0.1 M) supplemented with OsO_4 (1%) for 1 h at RT. Next, the cells were washed three times with Na-cacodylate buffer (0.1 M) followed. Then, the pellet was washed three times for 5 min with milliQ water and incubated overnight in Uranyl acetate buffer 1% (in water). Then, the sample was gradually dehydrated in ethanol (EtOH), at increasing concentration of 70%, 90%, 96% and 100%. Then, pellet was washed three times for 15 min with propylen oxide. Afterwards, the samples were incubated in a solution of Spurr and propylen oxide (1:3) and 3 h in Spurr and propylene oxide solution (1:1). Finally, the pellet was incubated for 3 h in Spurr and included into it by curing at 70°C overnight. Thin section of 70 nm of selected zones were observed with JEOL Jem1011 electron microscope operated at 100 keV.

Hyperthermia treatment experiments on the cells. For magnetic hyperthermia analyses of biological samples, approximately 3×10^6 IGROV-1 cells were seeded into a T25 flask (Corning®, New York, USA) with 3 ml of supplemented medium. After 24 h, the medium was replaced with 2 mL of fresh medium to which 50 µL of the IO23/48 particles at a final concentration of 0.2 g_{Fe}/L were added. After 48 h of incubation, the medium was removed, the cells were washed with PBS and detached with trypsin. The cells were counted using NucleoCounter® NC-100™ (ChemoMetec, Denmark) and 3×10^6 cells were transferred to small glass vial for the exposure to the hyperthermia treatment (MHT). A nanoScale DM100 Series (Biomagnetics Corp.) was used to generate the alternating magnetic field. The frequency was set at 182 kHz and the field was adjusted by the instrument in order to reach the user set temperature of 47°C. One single cycle of 90 minutes of hyperthermia was done (see Figure S14(b)).

PrestoBlue cell viability assay. The cell viability was studied using the commercially available PrestoBlue assay (Invitrogen, Carlsbad, CA, USA). Cytotoxicity assay was performed at different time points after cell treatment with nanoparticles and with (MHT) or without magnetic (w/o MHT) hyperthermia exposure. In detail, 70.000 cells per well were seeded in triplicate with 1 mL of fresh medium, into 24 multiwell plates. The PrestoBlue assay was carried out starting from 24 h following the hyperthermia treatment up to 72 h. After the desired incubation time, the medium was replaced by fresh medium supplemented with 10% PrestoBlue reagent and the cells incubated at 37 °C for 2 h in 5% CO_2. Afterwards, the medium of each experiment was transferred to a 96 multiwell plate and the absorbance of the solutions measured for 570 nm and 600 nm using a Multiskan™ FC Microplate Reader (Thermo Fisher Scientific, Waltham, MA, USA). The viability of each experiment was calculated considering the values measured for the control untreated cells (no nanoparticle and no hyperthermia exposure) as the 100% of viability.

The results were also compared to that of cell treated in the same way as above with nanoparticles but not exposed to magnetic hyperthermia treatment (w/o MHT).

Numerical simulations

Modelling the ACS spectra. The response of magnetic nanoparticles to an alternating magnetic field can be described using the complex Debye model, which is given by:

$$\chi(\omega) = \chi'(\omega) + i\chi''(\omega) \quad \text{Eq. S2}$$

$$\chi'(\omega) = \frac{\chi_0}{1 + (\omega\tau_e)^2} \quad \text{Eq. S3}$$

$$\chi''(\omega) = \frac{\chi_0 \omega\tau}{1 + (\omega\tau_e)^2} \quad \text{Eq. S4}$$

in which χ' and χ'' are the real and imaginary part of the ACS. By assigning an equal M_S and a cubic shape to all the particles, the imaginary part χ'' of the ACS spectra of nanoparticles, which relax *via* a mixture of Néel and Brownian mechanisms, can be described by a double integration over the particle core $f(d_c)$ and hydrodynamic $f(d_h)$ size distributions[8,9]:

$$\chi''(\omega) = \frac{1}{3}\chi_0^* \times \int_0^\infty f(d_h) \int_0^\infty \frac{\omega\tau_e}{1 + (\omega\tau_e)^2} \cdot d_c^6 \cdot f(d_c) dd_c dd_h \quad \text{Eq.S5}$$

in which

$$\chi_0^* = \frac{\mu_0 n M_s^2}{3k_B T} \quad \text{Eq. S6}$$

for cubic particles, given in the unit of volume m^3, μ_0 is the permeability of free space, M_s is the saturation magnetization, n is the particle number density, and k_B is the Boltzmann constant. The core and hydrodynamic size distributions were assumed to resemble a log-normal distribution function as given by

$$f(d_i,\mu_i,\sigma_i) = \frac{1}{\sqrt{2\pi}\sigma_i d_i} exp\left[-\frac{(\ln d_i - \ln \mu_i)^2}{2\sigma_i^2}\right] \quad \text{Eq.S7}$$

in which μ_i is the median particle size, and σ_i is the geometric standard deviation.

For the water-glycerol mixed samples, the Eq. S5 is modified to

$$\chi^{''}(\omega) = \frac{1}{3}\chi_0 \times \int_0^\infty \frac{\omega\tau_e}{1+(\omega\tau_e)^2} \cdot d_c^6 \cdot f(d_c) dd_c \quad \text{Eq.S8}$$

in which the integration is done only over the particle core. Note that a single mean value is estimated for η, and not a distribution.

The Brownian, Néel, and effective relaxation times at very low magnetic field amplitudes (*i.e.* 95 μT) are given by the following expressions[9,10].

$$\tau_B = \frac{3\eta d_H^3}{k_B T} \quad \text{Eq.S9}$$

$$\tau_N = \frac{\sqrt{\pi}}{2\sqrt{\frac{Kd_c^3}{k_B T}}} \tau_0 \exp\left(\frac{Kd_C^3}{k_B T}\right) \quad \text{Eq.S10}$$

$$\tau_e = \frac{\tau_B \tau_N}{\tau_B + \tau_N} \quad \text{Eq. S11}$$

in which K is the magnetocrystalline anisotropy constant, η is the viscosity of medium, and $\tau_0 = 10^{-9}\ s$ is the inverse attempt frequency.

The curve-fitting routine is based on the least squares regression method, exploiting the Levenberg-Marquardt algorithm as a robust scheme for non-linear problems. To estimate μ_h, σ_h, K, and M_s parameters, the ACS spectra of water-based samples were modelled using Eq. S5. In all the simulations, the core size distribution parameters (μ_c, σ_c) were set to the values that were obtained from the analysis of the TEM micrographs (Figure S1). The ACS spectra of the 41.5 wt%, 72.8 wt%, and 84.3 wt% glycerol samples were reconstructed using Eq. S8 wherein a single median μ_h, which was obtained from the analysis of the water-based samples, is assigned and μ_c and σ_c were set to TEM values. These calculations enabled an estimation of the mean η. M_s was estimated by setting χ_0^* (Eq. S6) as a free fit parameter into the simulations. The particle number density n (Eq. S6) was calculated from the ICP results by filling Fe and O atoms into a 23 nm large cubic Fe_3O_4 or FeO-Fe_3O_4 CS lattice structure when needed.

Note that the K values were estimated by setting V_m to the particle physical volume V_p in the magnetic energy barrier KV_m formula. As V_m is smaller than V_p for the biphasic particles, this could lead to an underestimation of K.

Therefore, the *K* values have to be considered comparatively and not absolutely.

Table S2. μ_h, σ_h, *K*, M_s, and *n* values which were obtained from the modelling of the ACS spectra.

notation	μ_h (nm)	σ_h	*K* (J/m^3)	M_s (kA/M)	*n* (μM)
IO23/0	42	0.25	2530	68	0.036
IO23/3	43	0.24	5500	152	0.036
IO23/6	43	0.25	5264	212	0.036
IO23/24	44	0.3	4200	260	0.036
IO23/48	53	0.38	3800	308	0.036

Reconstruction of the magnetization *M-H* curves. To derive the magnetic moment distribution from the *M-H* curves, they were reconstructed using MINORIM[11], a non-regularized inversion method which exploits a discrete form of the Langevin function given by

$$M(H_j) = \sum_{0}^{\infty} m_i L(m_i, H_j) n_i \qquad \text{Eq.S12}$$

$$L(m_i, H_j) = \coth\left(\frac{\mu_0 m_i H_j}{k_B T}\right) - \frac{k_B T}{\mu_0 m_i H_j} \qquad \text{Eq.S13}$$

in which m_i is the mean magnetic moment of i^{th} size bin with an amplitude equal to n_i, μ_0 is the permeability of the vacuum and k_B is the Boltzmann constant.[3]

This fit approach requires no *a priori* assumptions regarding the form and number of modality of the distribution function which is advantageous for an accurate determination of the magnetic moment distribution from the *M*-*H* curves. M_s and the mean magnetic moment m were set as fit parameters.

The exchange H_E and coercive H_C fields can be written as

$$H_E = \frac{-(H^+ + H^-)}{2} \quad \text{Eq.S14}$$

$$H_c = \frac{(H^+ - H^-)}{2} \quad \text{Eq.S15}$$

in which H^+ and H^- are the positive and negative coercivities taken from the field-cooled (FC) hysteresis loops.

Quantitative Rietveld crystal structure analysis. The Rietveld crystal structure method has been exploited to simulate the experimental XRD patterns, and to monitor the temporal evolution of the particle phase composition and lattice constant. The refinements were carried out using the FullProf Suite program. Firstly, the instrumental resolution function (IRF) file was generated by performing a profile matching on the LaB_6 NIST SRM 660a standard sample XRD pattern. The IRF file was uploaded into the program in order to take into account the instrumental broadening. The Thompson-Cox-

Hastings Pseudo-Voigt with an axial divergence asymmetry was selected as the peak shape. The background was set to a linear interpolation of background points which were obtained using the WinPLOTR software (FullProf package). The free parameters, which have shown more than a 50% cross correlation, were refined independently. The refined parameters were limited to the scale factor, lattice constants and the first two parameters of the anisotropic Lorentzian size broadening. To estimate the crystallite size, the Scherrer formula is written as

$$d = \frac{k\lambda}{\beta \cos(\theta)}$$

in which the anisotropy constants k_{220}=0.789 and k_{200}= 0.862 [12], =0.1540 nm is the wavelength of Cu-K_α, is the full maximum at half width (FWHM) and is the Bragg angle in radians. The peak shape was assumed to be Gaussian.

Table S3. Atom positions, sites, and occupancies used in the Rietveld analysis of the IO23 sample series for both FeO and Fe_3O_4 phases.

Fe_3O_4						
atom	valence	x	y	z	site	occupancy
Fe(t)	2+	0.125	0.125	0.125	8a	1
Fe(o)	3+	0.5	0.5	0.5	16d	1
O	2-	0.25	0.25	0.25	32e	1
FeO						
Fe	2+	0	0	0	4a	0.942
O	2-	0.5	0.5	0.5	4b	1

Further discussion on the Mössbauer results. The static Gaussian inhomogeneous broadenings of patterns #1 and #2 cannot be separated from the broadenings that were caused by collective spin fluctuations in the magnetic anisotropy potential of the particles.[13] Notably, we cannot observe fluctuations that cross the magnetic energy barrier even at 300 K. Note that the Néel relaxation peak at kHz frequency regime, as was observed in the ACS spectra (Figure 2), is far lower than the Mössbauer frequency. Thus, the superparamagnetic fluctuations that are traced by the ac-susceptibility appear static on the magnetic hyperfine splitting timescale seen by Mössbauer spectroscopy.

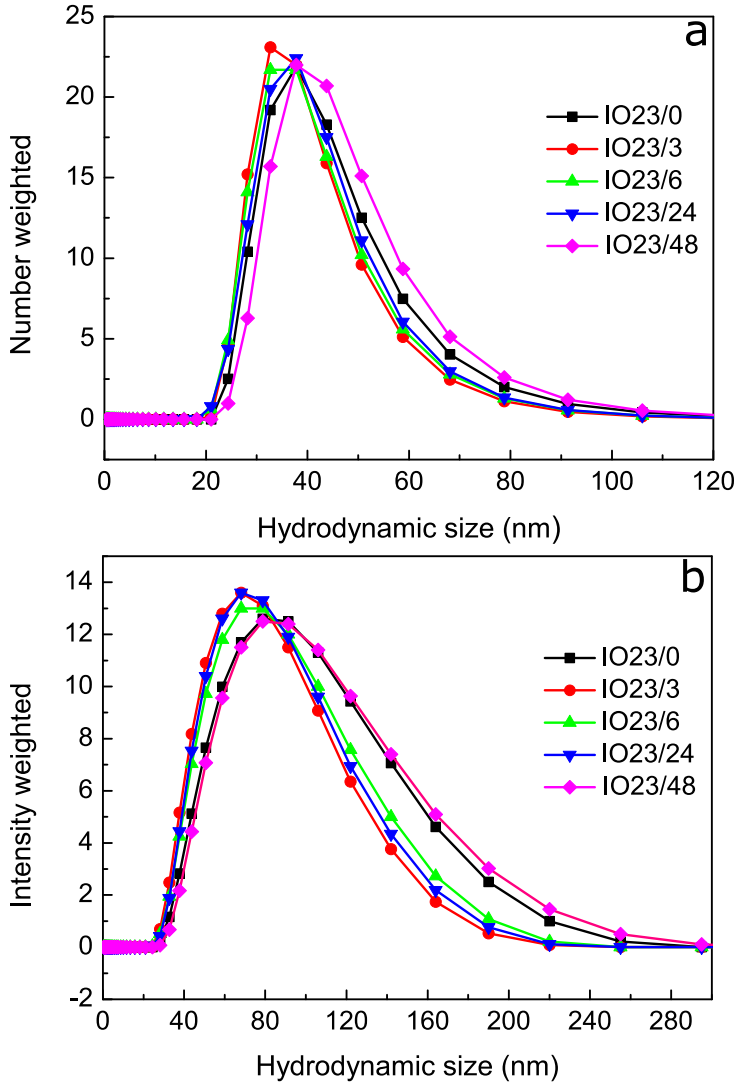

Figure S3. (a) The number-weighted and (b) the intensity-weighted hydrodynamic size distribution of the 23 nm sample series.

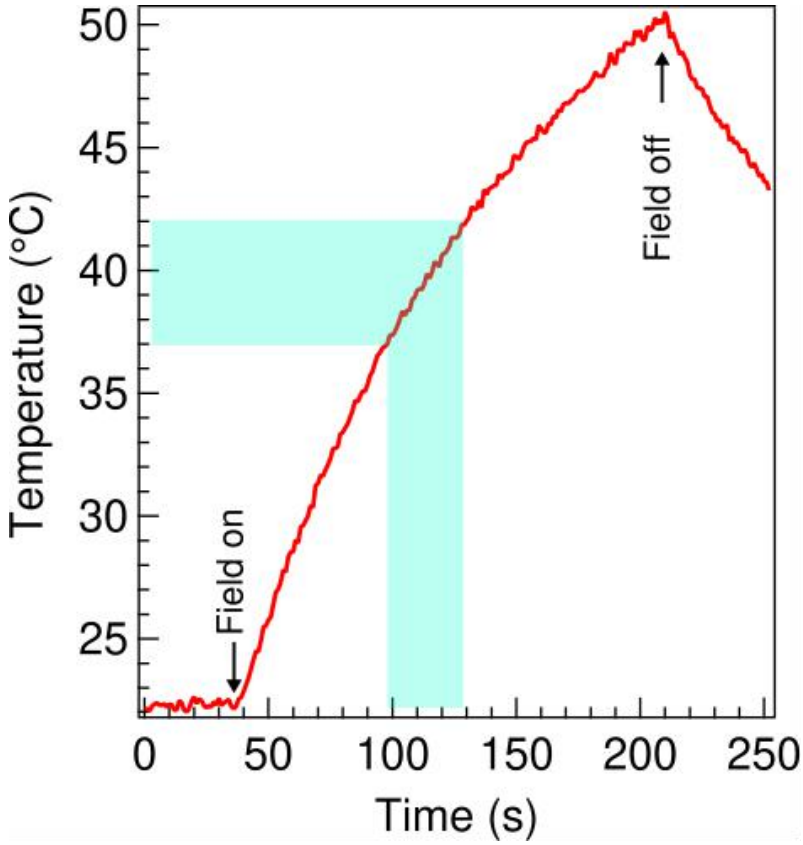

Figure S4. Typical calorimetric measurement of a magnetically induced temperature elevation versus an alternating magnetic field exposure time, recorded for the IO23/48 aqueous sample at 301 kHz and 24 kA/m. The graph indicates that it takes around 30 s to increase the temperature from 37°C to 42°C at 3.49 g_{Fe}/L.

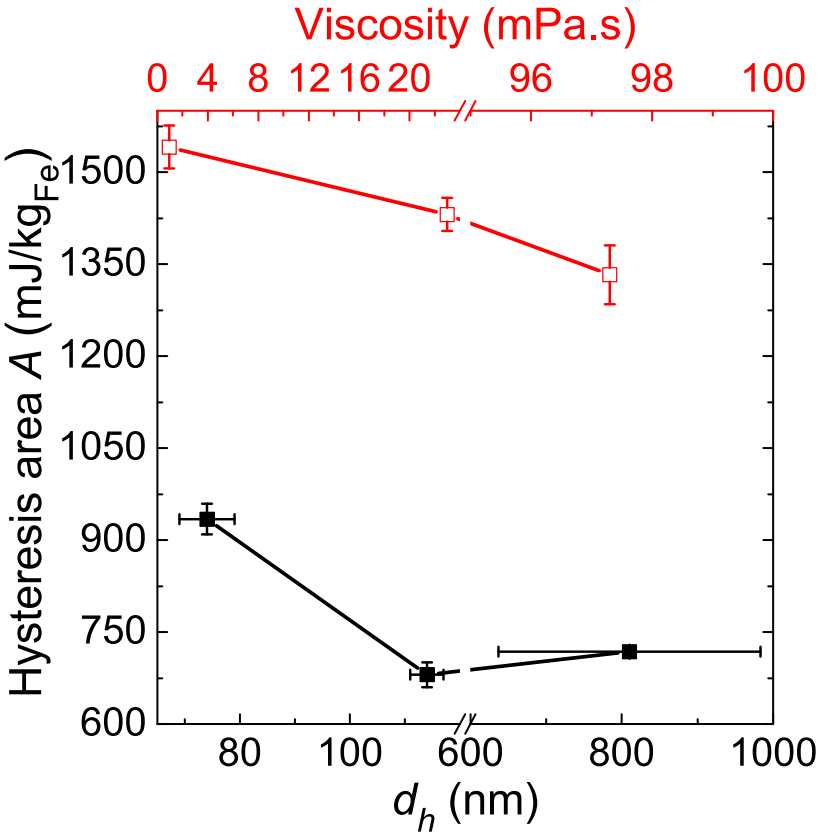
Viscosity (mPa.s)
0 4 8 12 16 20 96 98 100
Hysteresis area A (mJ/kg$_{Fe}$)
1500
1350
1200
1050
900
750
600
80 100 600 800 1000
d_h (nm)

Figure S5. Evolution of the AC loop area A ($\propto$SAR), derived from the AC loops shown in Figure 1 of the main text, as a function of the viscosity η and cluster hydrodynamic size d_h, which were recorded at 200 kHz and 100 kHz, respectively.

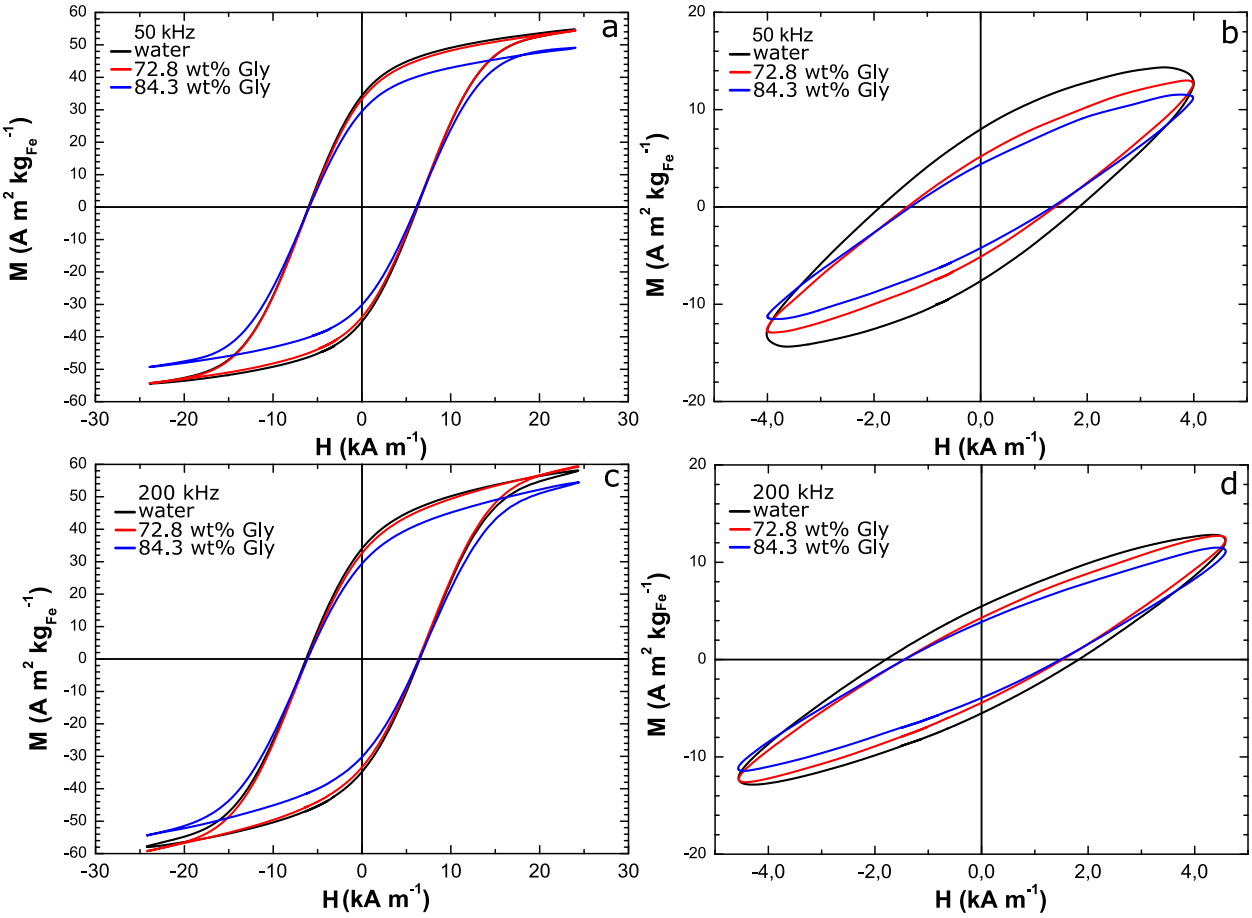

Figure S6. AC hysteresis loops recorded at (a) and (b) 50 kHz and (c) and (d) 200 kHz on the fully treated sample (IO23/48) in water and in high glycerol contents.

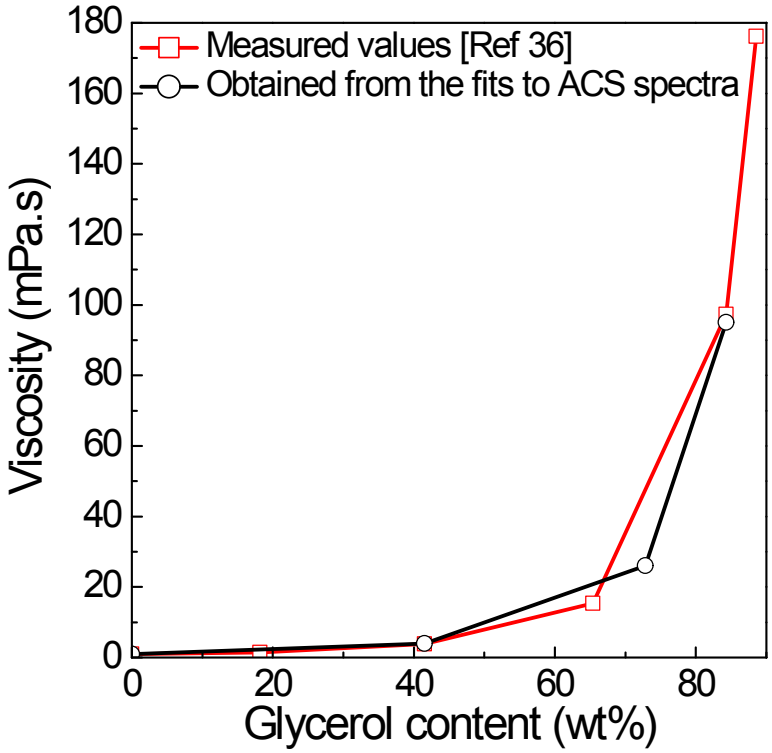

Figure S7. Measured and estimated viscosity of different water-glycerol mixtures. The viscosities were measured using a DH-2 rheometer (TA Instruments, Delaware, USA), as it is discussed in Ref. 39 of the main paper. The values were also obtained from the fits to the χ'' part of the ACS spectra (Figure 2b) using Eq. S8.

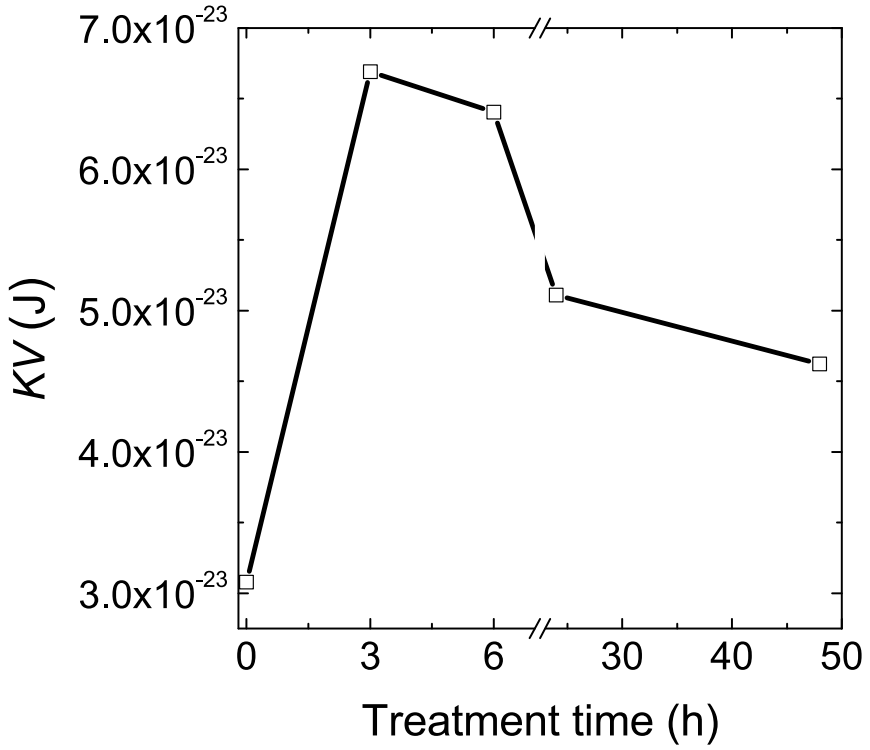

Figure S8. Evolution of the magnetic energy barrier KV_m *vs.* the thermal treatment time

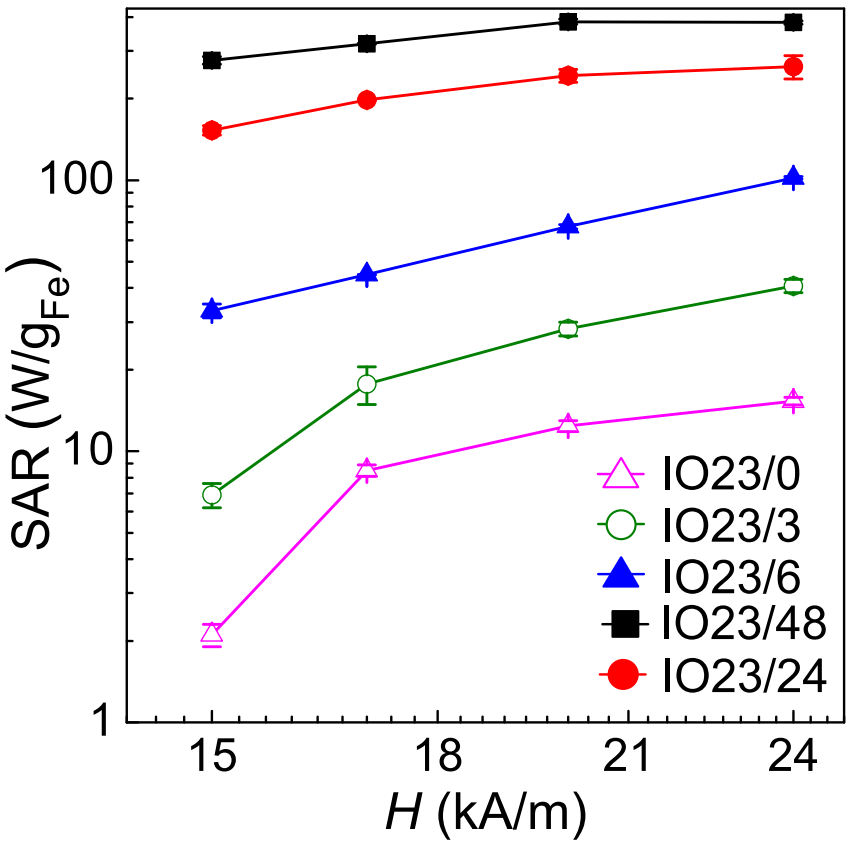

Figure S9. Double logarithmic plot of the magnetic field dependence of the SAR values. All samples were measured at 301 kHz.

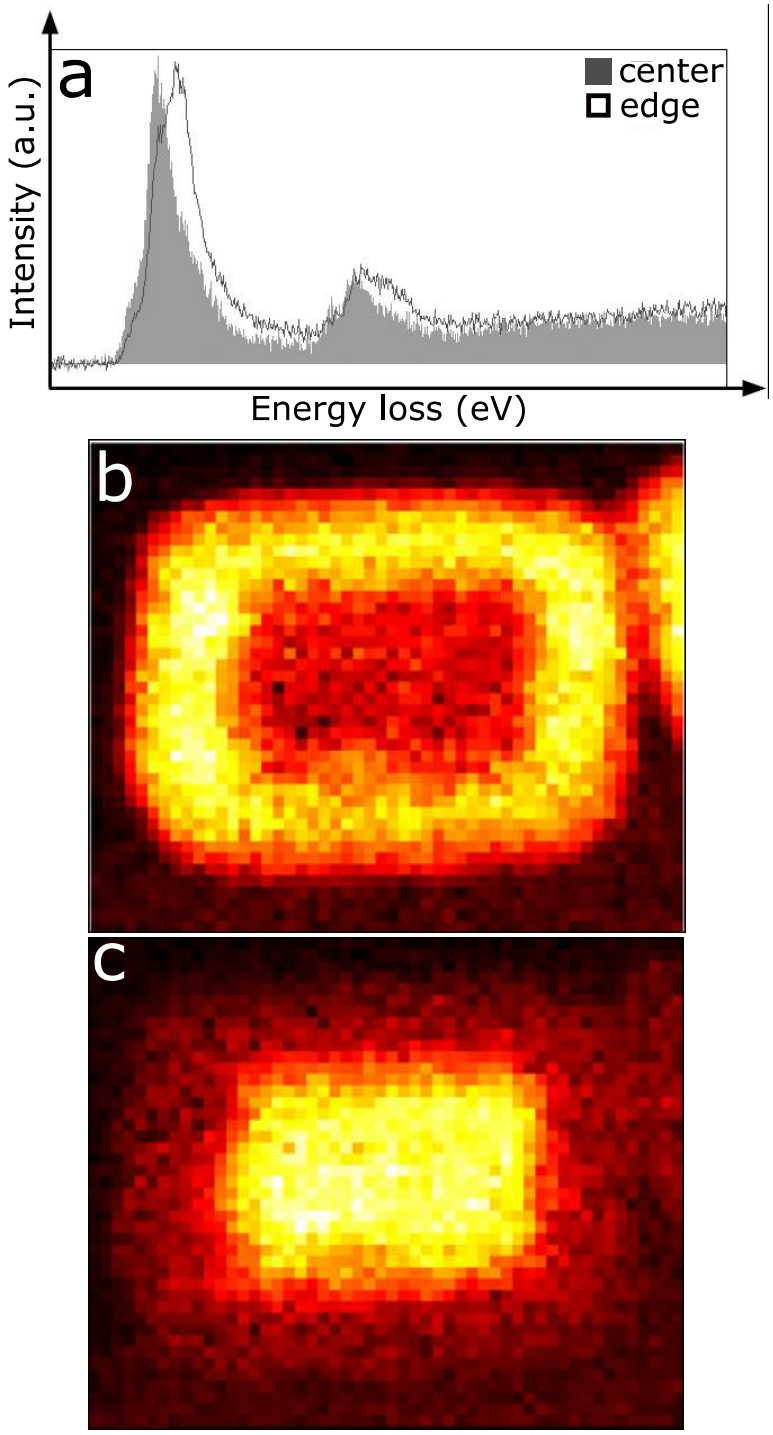

Figure S10. (a) EELS spectra acquired from the middle and near the edge of the as-prepared core-shell particle. The valency maps were obtained by

fitting the EELS spectra in each pixel to the reference spectra of Fe^{+3} (b) and Fe^{+2} (c).

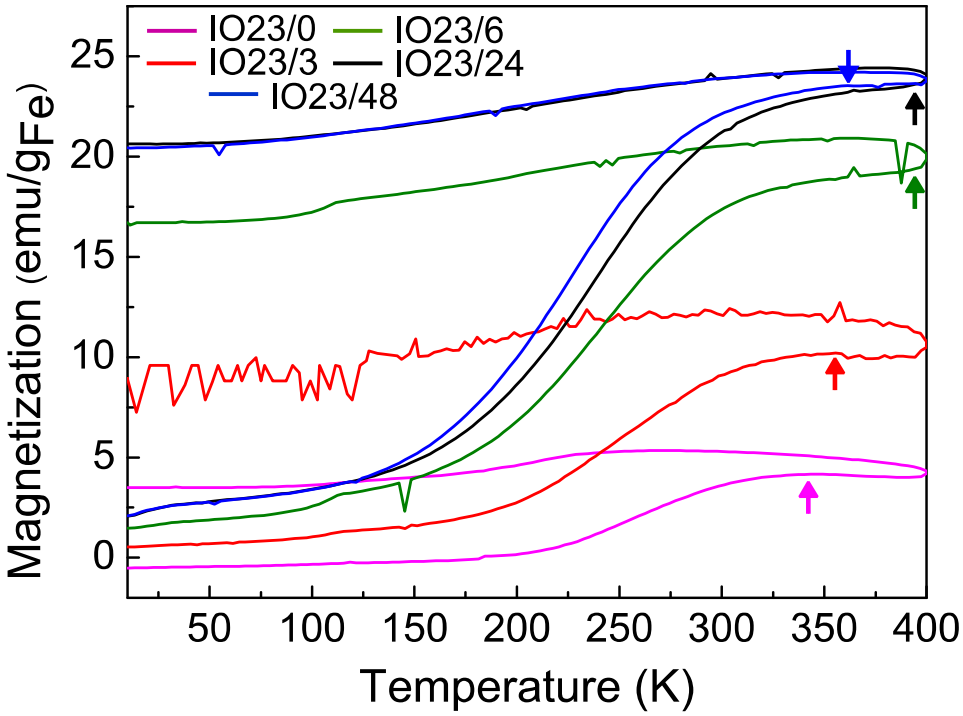

Figure S11. Temperature dependent zero-field and field-cooled ZFC-FC magnetization curves of the IO23 sample series, recorded at 5 mT warming-cooling fields. The maximum of the ZFC branch is marked with an arrow. The

ZFC maximum for the IO23/6 and IO23/24 samples seems to occur above 400 K.

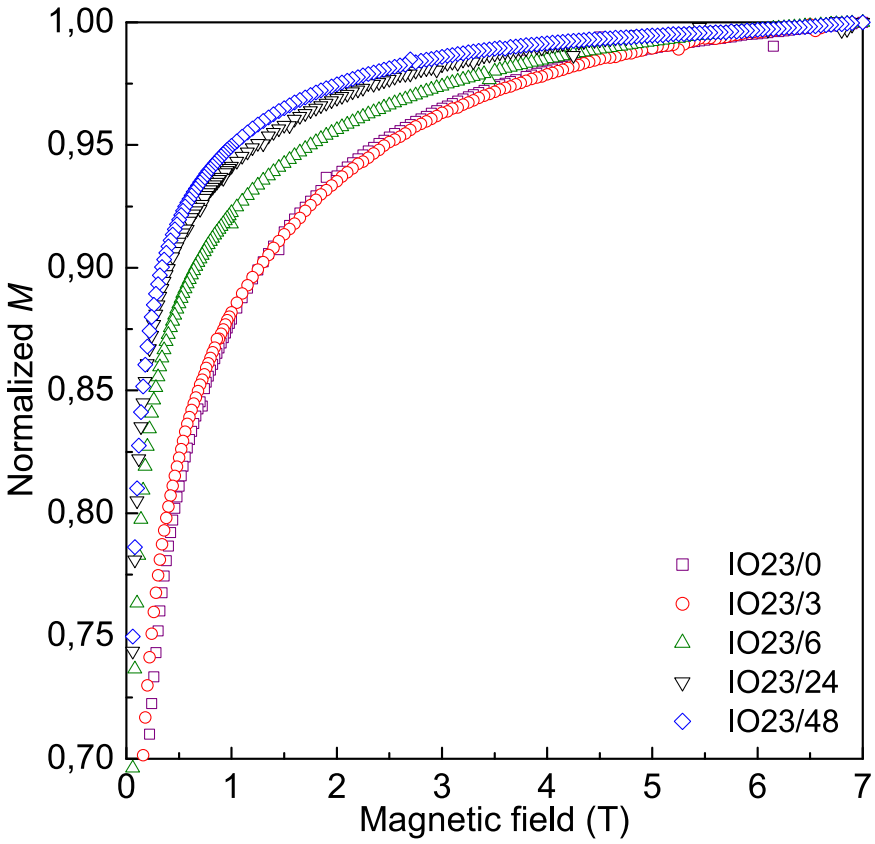

Figure S12. Normalized *M-H* curves of the 23 nm sample series, shown from 0 to 7 T. The full curves are presented in Figure 4 in the main paper.

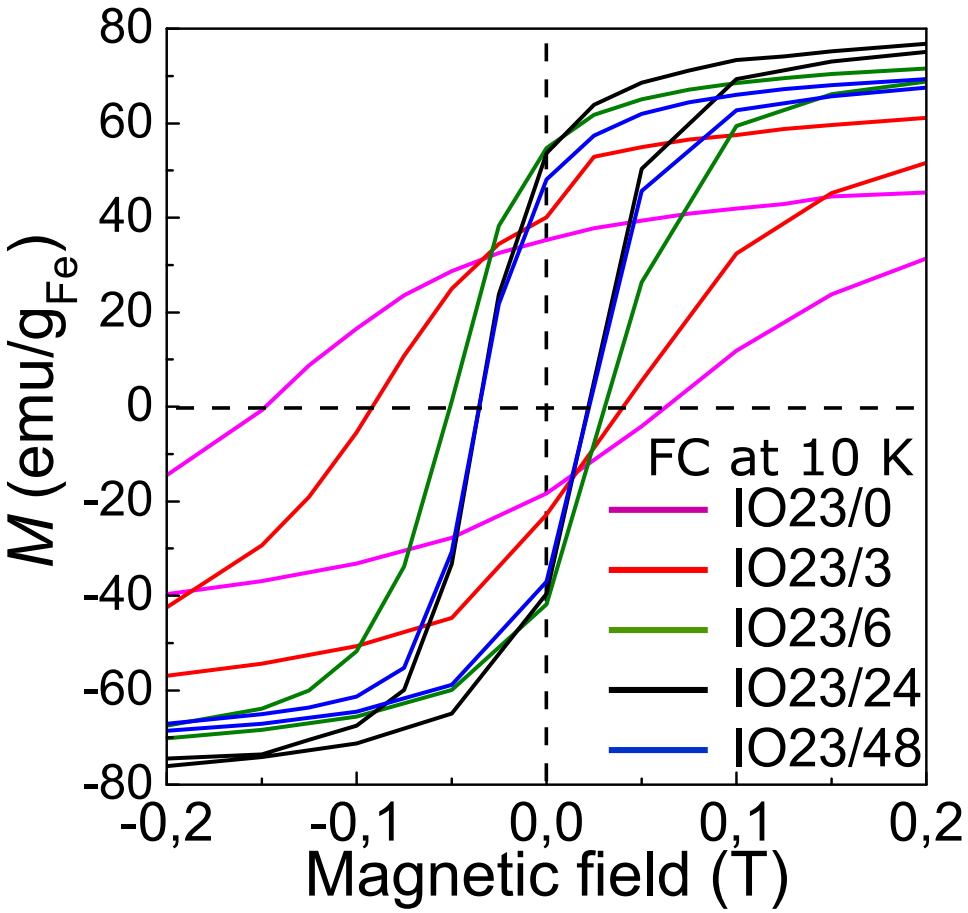

Figure S13. Field-cooled (FC) loops recorded at 10 K on the immobile IO23/48 nanocubes after cooling from 400 K to 10 K in 5 T magnetic fields.

(a)

Sample	µmol Fe / 10^6 cells
Cells	0.0005
IO23/48	0.45

Sample	mg Fe ad.	mg Fe in.	% in.
IO23/48	0.2	0.06	30

(b)

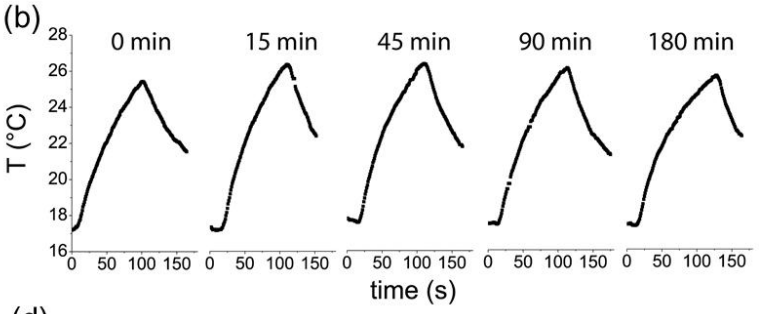

(c)

Sample	µmol Fe / 10^6 cells
Cells	0.0015
IO23/48	1.98

Sample	mg Fe ad.	mg Fe in.	% in.
IO23/48	0.4	0.3	75

(d)

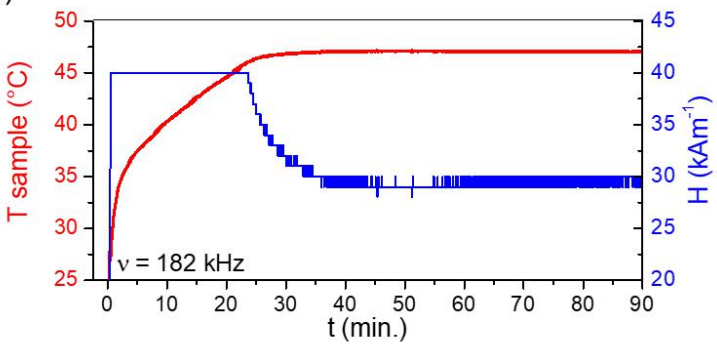

Figure S14. (a) Tabulated elemental analysis of iron associated to 5 million cells for the experiment shown in Figure 5a-b. The amount of iron from untreated cells, denoted here as cells, is reported as reference. (b) Heating profiles recorded on the IO23/48 particle/cell pellet mixture at different incubation intervals under the field frequency and amplitude of 301 kHz and 24 kA/m. (c) Tabulated elemental analysis of iron associated to 3 million cells for the experiment shown in Figure 5c-d. After 48 h of incubation time, a 75% of the administered dose

(ad.) of particles was found to be bound or internalized (in.) by the cells. (d) Temperature (T, red line) and field amplitude (H, blue line) profiles versus time (t) during the hyperthermia treatment of the IO23/48 doped cells. The field frequency was set constant to 182 kHz and the field amplitude was adjusted (blue curve) in a way to reach T_{max} of 47°C.

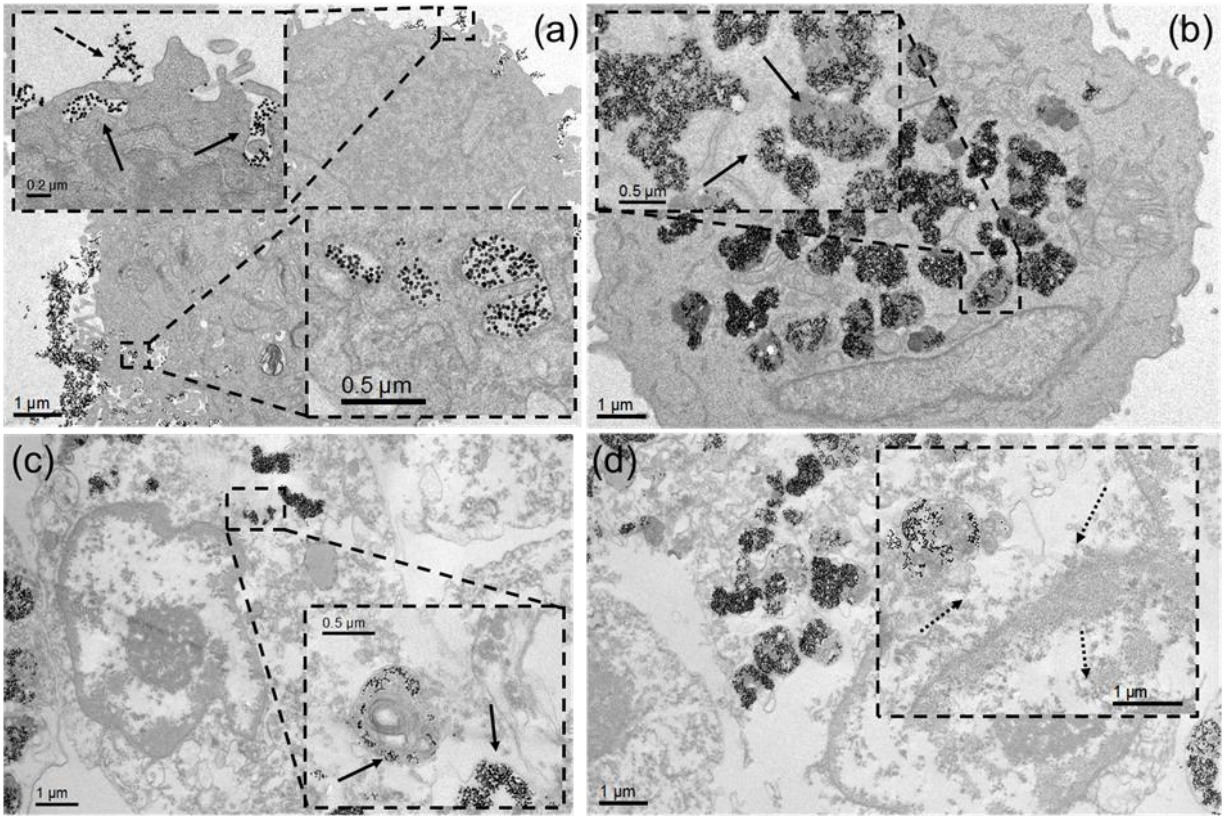

Figure S15. Thin-section TEM images of the IGROV-1 cells incubated with the IO23/48 nanocubes for (a) 180 minutes and (b) 48 h. (a) After 180 minutes, the particles are bound to the cell membrane (dashed black arrows) and are progressively internalized (solid black arrows). (b)

A consistent internalization of the particles is clearly seen after 48 h of incubation with the particles engulfed by the intracellular organelles (black arrows). (c) After hyperthermia treatment, the particles are still accumulated inside the intracellular organelles, which have a less defined structure due to the heat exposure (black arrows). (d) The hyperthermia treatment clearly compromises the intracellular organization and the typical cytosolic and nuclear structures appear to collapse completely (dotted black arrows).

References

(1) Lak, A.; Ludwig, F.; Scholtyssek, J. M.; Dieckhoff, J.; Fiege, K.; Schilling, M. Size Distribution and Magnetization Optimization of Single-Core Iron Oxide Nanoparticles by Exploiting Design of Experiment Methodology. *IEEE Trans. Magn.* **2013**, *49*, 201–207.

(2) Connord, V.; Mehdaoui, B.; Tan, R. P.; Carrey, J.; Respaud, M. An Air-Cooled Litz Wire Coil for Measuring the High Frequency Hysteresis Loops of Magnetic Samples - A Useful Setup for Magnetic Hyperthermia Applications. *Rev. Sci. Instrum.* **2014**, *85* (9).

(3) Schoenmakers, R. H. M.; Perquin, R. A.; Fliervoet, T. F.; Voorhout, W. High Resolution, High Throughput Electron Tomography Reconstruction. *Microsc. Microanal.* **2005**, *11*, 312–313.

(4) Schoenmakers, R. H. M.; Perquin, R. A.; Fliervoet, T. F.; Voorhout, W.; Schirmacher, H. New Software for High Resolution, High Throughput Electron Tomography. *Microsc. Anal.* **2005**, *19*, 5–6.

(5) Palenstijn, W. J.; Batenburg, K. J.; Sijbers, J. Performance Improvements

for Iterative Electron Tomography Reconstruction Using Graphics Processing Units (GPUs). *J. Struct. Biol.* **2011**, *176*, 250–253.

(6) Van Aarle, W.; Palenstijn, W. J.; De Beenhouwer, J.; Altantzis, T.; Bals, S.; Batenburg, K. J.; Sijbers, J. The ASTRA Toolbox: A Platform for Advanced Algorithm Development in Electron Tomography. *Ultramicroscopy* **2015**, *157*, 35–47.

(7) Quarta, A.; Rodio, M.; Cassani, M.; Gigli, G.; Pellegrino, T.; Del Mercato, L. L. Multilayered Magnetic Nanobeads for the Delivery of Peptides Molecules Triggered by Intracellular Proteases. *ACS Appl. Mater. Interfaces* **2017**, *9*, 35095–35104.

(8) Chung, S. H.; Hoffmann, A.; Guslienko, K.; Bader, S. D.; Liu, C.; Kay, B.; Makowski, L.; Chen, L. Biological Sensing with Magnetic Nanoparticles Using Brownian Relaxation (Invited). *J. Appl. Phys.* **2005**, *97* (10).

(9) Ludwig, F.; Guillaume, A.; Schilling, M.; Frickel, N.; Schmidt, A. M. Determination of Core and Hydrodynamic Size Distributions of CoFe2O4 Nanoparticle Suspensions Using Ac Susceptibility Measurements. *J. Appl. Phys.* **2010**, *108*, 033918.

(10) Cabrera, D.; Lak, A.; Yoshida, T.; Materia, M. E.; Ortega, D.; Ludwig, F.; Guardia, P.; Sathya, A.; Pellegrino, T.; Teran, F. J. Unraveling Viscosity Effects on the Hysteresis Losses of Magnetic Nanocubes. *Nanoscale* **2017**, *9*, 5094–5101.

(11) van Rijssel, J.; Kuipers, B. W. M.; Erné, B. H. Non-Regularized Inversion Method from Light Scattering Applied to Ferrofluid Magnetization

Curves for Magnetic Size Distribution Analysis. *J. Magn. Magn. Mater.* **2014**, *353*, 110–115.

(12) Li, Z. Characterization of Different Shaped Nanocrystallites Using X-Ray Diffraction Line Profiles. *Part. Part. Syst. Charact.* **2012**, *28*, 19–24.

(13) Mørup, S.; Tronc, E. Superparamagnetic Relaxation of Weakly Interacting Particles. *Phys. Rev. Lett.* **1994**, *72*, 3278–3281.